BRNO UNIVERSITY OF TECHNOLOGY
VYSOKÉ UČENÍ TECHNICKÉ V BRNĚ

FACULTY OF MECHANICAL ENGINEERING
FAKULTA STROJNÍHO INŽENÝRSTVÍ

INSTITUTE OF PHYSICAL ENGINEERING
ÚSTAV FYZIKÁLNÍHO INŽENÝRSTVÍ

INFRARED MAGNETO-SPECTROSCOPY OF BI$_2$TE$_3$ TOPOLOGICAL INSULATOR
INFRAČERVENÁ MAGNETO-SPEKTROSKOPIE TOPOLOGICKÉHO IZOLÁTORU BI$_2$TE$_3$

MASTER'S THESIS
DIPLOMOVÁ PRÁCE

AUTHOR   Bc. Ivan Mohelský
AUTOR PRÁCE

SUPERVISOR   Milan Orlita, Ph.D.
VEDOUCÍ PRÁCE

BRNO 2020

Specification Master's Thesis

Department:	Institute of Physical Engineering
Student:	**Bc. Ivan Mohelský**
Study programme:	Applied Sciences in Engineering
Study field:	Physical Engineering and Nanotechnology
Supervisor:	**RNDr. Milan Orlita, Ph.D.**
Academic year:	2019/20

Pursuant to Act no. 111/1998 concerning universities and the BUT study and examination rules, you have been assigned the following topic by the institute director Master's Thesis:

Infrared magneto–spectroscopy of Bi2Te3 topological insulator

Concise characteristic of the task:

The Bi2Te3 semiconductor belongs to the steadily expanding class of time–reversal–invariant 3D topological insulators. These recently emerged materials are characterized by a well–defined energy band gap in bulk, but with metallic (gapless) states on the surface, with relativistic–like (linear in momentum) dispersion of electrons. Despite considerable effort, the electronic band in bulk Bi2Te3 remain to be a source of controversy. For instance, there has been no consensus established about the band parameters of the energy band gap (width & direct/indirect nature).

In the proposed Master thesis, the Bi2Te3 topological insulator (and others material of interest from this class) will be explored in a close collaboration between BUT and Laboratoire National des Champs Magnétiques Intenses (LNCMI) CNRS in Grenoble. The primary technique, infrared magento–spectroscopy (Grenoble) will be combined with magneto–transport experiments and zero–field optical measurements in laboratories at the CEITEC–Nano.

Goals Master's Thesis:

1. To prepare a consise review about the current–state of knowledge of Bi2Te3 physical properties (electronic band structure in theoretical first–principles studies and in experiments: optics, ARPES, transport, recent progress in the field).
2. To realize magneto–optical measurements (LNCMI–Grenoble) on thin layers of of Bi2Te3 (JKU Linz) and other topological systems (CEITEC), magneto–infrared and –transport studied (CEITEC).
3. To analyze/model/interpret the obtained experimental data (specific goal: clarifying the width and nature of the energy band gap in Bi2Te3).

Recommended bibliography:

ORLITA, M., B.A. PIOT, G. MARTINEZ, et al. Magneto-Optics of Massive Dirac Fermions in Bulk Bi 2 Se 3. Physical Review Letters. 2015, 114(18).

DUBROKA, A., O. CAHA, M. HRONČEK, et al. Interband absorption edge in the topological insulators Bi 2 (Te 1 − x Se x) 3. Physical Review B. 2017, 96(23).

NECHAEV, I. A. a E. V. CHULKOV. Quasiparticle band gap in the topological insulator Bi 2 Te 3. Physical Review B. 2013, 88(16).

KÖHLER, H. Non-ParabolicE(k) Relation of the Lowest Conduction Band in Bi2 Te3. Physica status solidi (b). 1976, 73(1), 95-104.

Deadline for submission Master's Thesis is given by the Schedule of the Academic year 2019/20

In Brno,

L. S.

....
prof. RNDr. Tomáš Šikola, CSc.   doc. Ing. Jaroslav Katolický, Ph.D.
Director of the Institute   FME dean

Abstract

The main goal of this thesis is to characterize the electronic band structure of Bi_2Te_3 topological insulator, a system that is, in an ideal case, insulating in bulk but conducting via metallic surface states. This material has been extensively studied for more than 60 years, however, its bulk band structure is not yet fully understood, especially the characteristics of the band gap are still a matter of discussion. In this thesis, results of a Landau level spectroscopy in magnetic fields up to 34 T, supplemented by ellipsometry at zero magnetic field, are presented to clarify some of the band gap properties. The observed response is consistent with the picture of a direct-gap semiconductor in which charge carriers closely resemble massive Dirac particles. The fundamental band gap reaches $E_g = (175 \pm 5)$ meV at low temperatures, and it is not located on the trigonal axis, thus displaying either six or twelvefold valley degeneracy.

Abstrakt

Tato práce se zabývá charakterizací topologického izolátoru Bi_2Te_3, materiálu s nevodivými stavy v objemu, ale jedním vodivým pásem na povrchu. Tento materiál je zkoumán již přes 60 let, ale i přes to není jeho objemová pásová struktura úplně objasněna, obzvláště charakter zakázaného pásu je stále předmětem diskuze. V této práci jsou prezentovány výsledky infračervené spektroskopie na Landauových hladinách v magnetickém poli až do 34 T, doplněné elipsometrickým měřením mimo magnetické pole. Výsledky těchto měření by měli pomoci vyjasnit některé vlastnosti zakázaného pásu. Pozorovaná optická odezva odpovídá polovodiči s přímým zakázaným pásem, ve kterém se nosiče náboje chovají jako Diracovské hmotné fermiony. Šířka zakázaného pásu za nízkých teplot byla určena jako $E_g = (175 \pm 5)$ meV a samotný zakázaný pás se nachází mimo trigonální osu, tím pádem se v první Brillouinově zóně vyskytuje 6 krát nebo 12 krát.

Keywords
bismuth telluride, topological insulator, magneto-optics, Fourier-transform infrared spectroscopy, Landau levels, cyclotron resonance

Klíčová slova
Tellurid bismutitý, topologický izolátor, magneto-optika, Fourierovská infračervená spektroskopie, Landauovy hladiny, cyklotronová rezonance

I hereby declare that I have written my master's thesis on the theme of *Infrared magneto-spectroscopy of Bi_2Te_3 topological insulator* independently, under the guidance of the master's thesis supervisor, Milan Orlita, Ph.D., and using the technical literature and other sources of information which are all properly quoted in the thesis and detailed in the list of literature at the end of the thesis.

....
Place and date   Bc. Ivan Mohelský

ACKNOWLEDGMENT

I would like to thank my thesis supervisor Dr. Milan Orlita, who together with his Ph.D. student Jan Wyzula, introduced me to magneto-optical spectroscopy as well as physics of topological insulators. I am very grateful for their time spent answering countless of my questions and proofreading this thesis. I am also very thankful to the rest of the Nanophysics group at the LNCMI led by Marek Potemski, namely Yuriy Krupko, who performed the magneto-transport experiment and Diana Václavková with whom I shared an office and many laughs. I would also like to thank my family, who supported me through the whole five years of me attending university and my girlfriend Kateřina who is the most tolerant person I have ever met and was always able to cheer me up when I needed to. I also may not omit my colleagues from Physical engineering, who made the five years spent at the university more fun than I have ever expected. Finally, my thanks go to the English rock band Pink Floyd that accompanied me through the whole process of writing this thesis.

Bc. Ivan Mohelský

Contents

1. Introduction

Our understanding of condensed matter and the especially solid-state matter is constantly evolving as new properties of solids are being discovered. Some, like superconductivity, have already been broadly implemented in today's technology. Others, like spin waves that are predicted to revolutionize data processing and logical gates, still await their first application. One such novel phase of solid-state matter is topological insulators, materials insulating in bulk, but hosting specific metallic states on the surface.

One of the first identified 3D topological insulators was a bismuth telluride, a narrow gap semiconductor with a single linear gapless band on the surface. Intensive investigations of Bi_2Te_3 have started more than sixty years ago, and they were mostly driven by its unusual thermoelectric properties. Currently, it is a working material of most Peltier devices. Despite being a subject of extensive research, further fostered by the discovery of specific relativistic-like surface states, its band structure is, to this day, only partially understood. In this thesis, the band structure of Bi_2Te_3 will be studied with a purpose of clarification of some of its band gap characteristics.

The primary tool used for this goal is magneto-optical spectroscopy, a technique using an external magnetic field to induce changes in the band structure of studied material, allowing us to study phenomena in solids. The applied magnetic field represents an additional, widely tunable parameter that allows us to get, for instance, deeper (and more precise in the quantitative sense) insights into the electronic band structure of various solids. Landau level spectroscopy studies effects related to the quantization of electronic bands, into so-called Landau levels, by the applied magnetic field. An analysis of electron excitations between the Landau levels may help us to reconstruct the band structure of the studied material.

This thesis is divided into six chapters. The second chapter of this thesis is dedicated to an overview of topological insulators, with a focus on Bi_2Te_3. In particular, current knowledge about its electronic band structure is reviewed. In the third chapter, an optical response of solids in a magnetic field is discussed, and a model of Dirac massive fermions is adopted and described. In the fourth chapter, an experimental setup for Landau level spectroscopy is described, comprising of Fourier-transform infrared spectrometer and different types of magnets. In the fifth chapter, we present and discuss our recently published experimental results from Landau level spectroscopy and ellipsometry of Bi_2Te_3 [1] and magneto-transport measurements of ScPtBi thin layers.

This thesis was accomplished in cooperation of Brno University of Technology and The Laboratoire National des Champs Magnétiques Intenses (LNCMI) in Grenoble, France.

1. INTRODUCTION

2. Topological insulators

In solid-state physics, materials are divided into two general groups according to their ability to conduct electrical current. The origin of these characteristics was traced to the most fundamental property of matter, its electronic band structure, and its occupation by electrons. Materials that do not form an energy gap in their band structure can conduct charge and are called conductors – opposite to those with the band gap that are called insulators.

There are materials at the border between metals and insulators. These comprise systems with relatively small gaps (semiconductors) and vanishing gaps, but relatively small carrier densities (semimetals). One of the definitions describes semiconductors as materials with an energy gap that is non-zero but does not exceed a few electronvolts [2].

This definition of basic material groups held well for a long time until new phases of materials started to emerge. Topological insulators represent one of such new phases. These are systems with a well-defined band gap in the bulk band structure, but they also comprise some symmetry-protected conducting states on the surface [3]. This effect was first observed in 2007 for HgTe quantum wells only a year after its theoretical prediction. Soon after, 3D topological insulators were discovered experimentally. These are bulk systems with specific two-dimensional relativistic-like (gapless) surface states.

Such 2D surface states may appear in systems with so-called band inversion, which refers to the ordering of bands different from that of atomic orbitals in a vacuum, and with strong spin-orbital interaction. Therefore, materials containing heavy elements exhibiting strong spin-orbital interaction like mercury or bismuth are possible candidates to exhibit these topological properties.

2.1. Quantum spin Hall insulators

The quantum Hall effect refers to quantized conduction of 2D systems in the magnetic field. When a sufficiently strong magnetic field is applied to the system confined to only two dimensions, its electrons start to perform a circular motion (Figure 2.1 a)).

These electrons can only occupy orbits with discrete and strongly degenerated energy values, called Landau levels. Both the energy and degeneracy of Landau levels are directly proportional to the intensity of the applied magnetic field, and therefore, whether the Fermi level lies inside the Landau level or inside a gap between them changes with an increasing magnetic field (Figure 2.1 b)). Just like in regular conductor/insulator, the position of the Fermi level determines the ability to conduct electrons. When the Fermi level is inside the Landau level, the material acts as a conductor, on the other hand, when the Fermi level is in the gap between the Landau levels, there are no electrons to conduct and the material acts as an insulator. However, it was found that even in such a case, there are still some electrons traveling through the material, but only in one direction
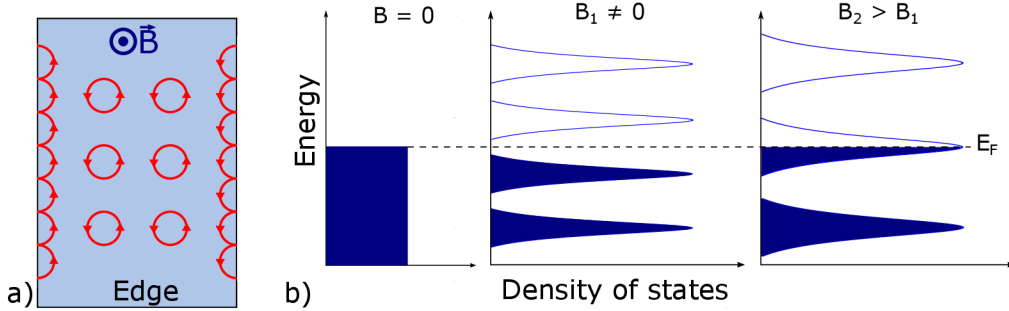
Figure 2.1: a) Electrons in a magnetic field perform cyclotron motion in a quantized band structure of a 2D system. There are "bulk" states dependent on the magnetic field and position of the Fermi level and states at the boundary of the system, where electrons can travel in one direction along the edge independently on the magnetic field. b) The quantization of band structure into Landau levels due to the magnetic field with the energy and degeneracy that both increase with the applied magnetic field.

along the edges, and the conductivity of such electrons is quantized as $G = n\frac{e^2}{h}$, where n is an integer (filling factor), e is a charge of an electron and h is Planck constant.

The cyclotron motion of some electrons is interrupted at a boundary of the system. These electrons "bounce" of the edge and travel along the boundary. Such "skipping orbits" leads to states that are not quantized by the magnetic field and propagate in only one direction. Not only are these states able to participate in electron transport, but as the transport is unidirectional, the electrons do not scatter and do not dissipate any energy, resulting in a perfect and precisely quantized transport.

However, quantized transport of electrons through edge states, as is the case of the quantum Hall effect, also occurs without the magnetic field being applied. In 2006, Bernevig, Hughes and Zhang [4] proposed that a similar effect, called quantum spin Hall effect, may appear in a specific class of 2D materials at $B = 0$, and called them topological insulators. The magnetic field is substituted by spin-orbit coupling, an interaction of electron's intrinsic angular momentum, or spin, with the orbital motion of the electrons. The spin-orbital interaction is stronger in atoms with a high atomic number, and therefore electrons in heavier atoms exhibit stronger spin and momentum dependent coupling, which, to a certain extent, resembles the application of the magnetic field. As the spin-orbit coupling depends on the spin of an electron, the electron transport due to topological states, in a quantum spin Hall effect, is spin-polarized. Therefore, the direction of transport also depends on the spin of the electron. That is why topological insulators in two-dimensions are referred to as quantum spin Hall insulators.

While the first proposition to observe the quantum spin Hall effect was in graphene, it appeared unrealistic due to its too weak spin-orbit coupling. HgTe quantum well (Figure 2.2 a)) was the second system proposed to exhibit the quantum spin Hall effect. It was predicted to undergo a topological phase transition (band inversion, Figure 2.2 b)) as the band gap closes at thickness $d_c > 6.4\,\text{nm}$ and reopens with the inverted ordering of bands for $d > d_c$. In the inverted regime, the system was calculated to exhibit the quantum Hall effect in the absence of the external magnetic field with spin-polarized electron transport [4].

This phase was also predicted by Pankratov and Volkov [5] in 1987 in a $Pb_{1-x}Sn_xTe$ and $Hg_{1-x}Cd_xTe$ heterojunctions. These are other systems, in which a particular com-
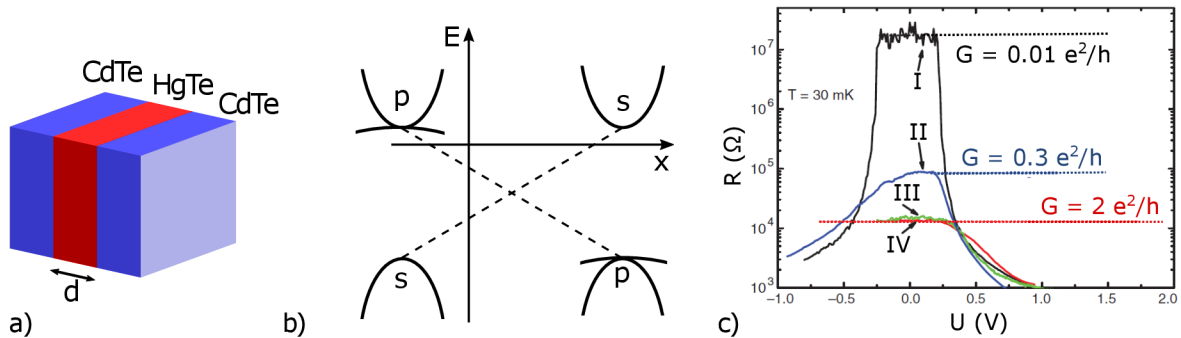
Figure 2.2: a) Schema of a HgTe quantum well of a thickness d. b) Calculation of band inversion of $Hg_{1-x}Cd_xTe$, in dependence on x, adapted from [5]. c) Measurement of resistance of HgTe quantum well presented by Konig at al. [6], where samples I and II have thickness $d < d_c$ and show insulating properties while samples III and IV exhibit quantum spin Hall state, showing quantized conductance $G = \frac{2e^2}{h}$.

position x (relatively high concentration of Sn or Hg) may give rise to band inversion. Pankratov and Volkov predicted that, at the interface of an inverted and non-inverted material, 2D electronic states with a linear energy dispersion on the wave vector k should exist.

The quantum spin Hall effect was experimentally confirmed only one year after its theoretical prediction. König et al. [6] reported electron transport measurement on the HgTe quantum wells with varying thickness d. They show that the quantum wells undergo a band inversion around $d_c = 6.3\,\text{nm}$, where the conductance is almost zero in the conventional non-inverted regime, but after the band inversion ($d > 6.3\,\text{nm}$), the conductance approaches $G = \frac{2e^2}{h}$. Figure 2.2 c) shows a measurement of four samples. Samples I and II have thickness $d < d_c$ and exhibit classical insulating properties, and samples III and IV with $d > d_c$ support the quantum spin Hall state with a quantized conductance. As the residual conductance stays constant with variations of the sample dimensions, the existence of the edge states of the quantum spin Hall insulator was confirmed.

2.2. 3D topological insulators

Soon after the confirmation of the edge states, many theorists independently came up with a three-dimensional generalization of the 2D quantum spin Hall insulator state [7–9] and the term topological insulator was first used [8]. After this, many materials were predicted to exhibit such properties, e.g.: $Bi_{1-x}Sb_x$, strained HgTe and α-Sn [7].

$Bi_{1-x}Sb_x$ alloy was the first experimentally confirmed 3D topological insulator [10]. Semimetallic bismuth and bismuth-based materials exhibit strong spin-orbital interaction making it an ideal candidate for a topological insulator. The valence and conductance bands at the L point of the Brillouin zone shows a nearly linear (apart from a small gap) dispersion that may be described by a (massive) Dirac equation [11]. When the Bi atoms are substituted by antimony, the gap between these bands gets smaller and at concentration $x \approx 0.04$, the gap closes completely and massless 3D Dirac point appears. Increasing the Sb concentration further reopens the gap with inverted ordering of bands (similar to the HgTe quantum wells [4]). This band inversion is depicted in Figure 2.3 a). At $x \approx 0.09$, the system becomes a direct-gap insulator with inverted massive Dirac bulk

5

bands and hosts metallic states on its surface (Figure 2.3 b)). When the Sb concentration is increased further, at $x \approx 0.22$ the system returns to the semimetallic state.
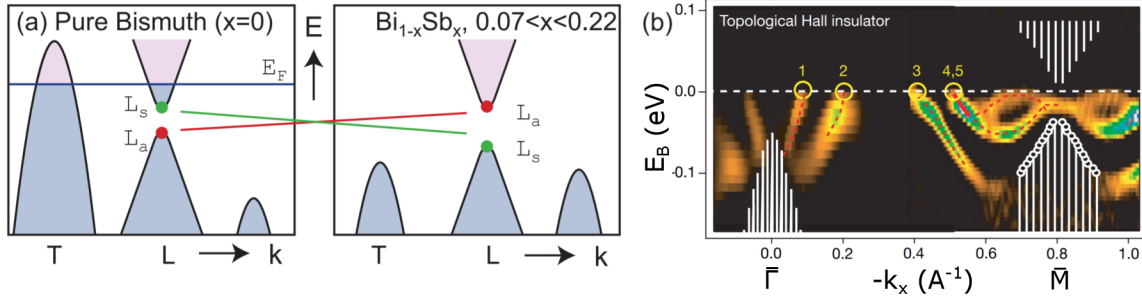

Figure 2.3: a) Schematic of a Bi band structure evolution with Sb doping. The band inversion of the almost linear bands at the L point of the Brillouin zone occurs at the Sb concentration $x \approx 0.07$. Adapted from [3]. b) ARPES measurement of the 111-face of $Bi_{0.9}Sb_{0.1}$, showing occupied surface states on the line between $\overline{\Gamma}$ and $\overline{M}$ points in the surface Brillouin zone. Adapted from [10].

Electron transport measurements, crucial in the identification of surface states in 2D systems [6], are much more problematic in the 3D, as it is difficult to separate the surface and bulk conductivity. In 2008, Hsieh at al. [10] have published results of angle-resolved photoemission spectroscopy (ARPES) of $Bi_{1-x}Sb_x$, directly observing the occupied electron states on the surface as a function of its energy and momentum. They found two gapless surface states near the $\overline{\Gamma}$ point (of the surface Brillouin zone) and additional gapless states near the $\overline{M}$ point, shown in Figure 2.3 b). The surface states in the ARPES measurements are easily distinguished from the bulk states as they do not disperse in the direction perpendicular to the surface. From that moment, ARPES technique has become a primary tool in search and identification of surface states and 3D topological insulators.

2.2.1. Bi-Se-Te Family

The second generation of 3D topological insulators [12] was discovered soon after the $Bi_{1-x}Sb_x$, containing mainly Bi_2Se_3 and Bi_2Te_3 compounds. Even though the surface states observed in these materials are, in principle, of the same origin, these materials hold certain advantages. Their surface states are considerably simpler, just a single cone (schematically pictured in Figure 2.4a)) at the $\overline{\Gamma}$ point as compared to the complex surface state structure with five electron bands in $Bi_{1-x}Sb_x$ alloy, that also has significantly smaller band gap.

The first observation of a conical band on the surface of Bi_2Se_3 was reported in a high-resolution ARPES study presented by Xia et al. [13]. The ARPES data were complemented by band structure calculations and identified the nearly linear dispersing band in Figure 2.4 c) as the topological surface states and the U-like feature as a bottom of the conduction band. Their measurement shows a single, non-degenerate surface state with almost linear dispersion (Figure 2.4 c), along both k_x and k_y directions with very similar band velocities $v \approx 5 \times 10^5 \, \text{ms}^{-1}$. As Bi_2Se_3 is a stoichiometric compound, it can, in principle, be prepared in much higher quality as compared to the $Bi_{0.9}Sb_{0.1}$ presented by Hsieh et al. in [10]. Another advantage over the $Bi_{1-x}Sb_x$ is its much larger band gap. The exact value and nature of the bulk band gap were, in fact, for a long time a matter of discussion as results of different techniques and band structure calculations

fell into rather broad range $E_\mathrm{g} = (200 - 300)$ meV. In 2017, Martinez et al. presented a combination of photoluminescence, transmission and electron transport measurements resulting in a conclusion of a direct band gap of energy $E_\mathrm{g} = (220 \pm 5)$ meV at the Γ point of the Brillouin zone [14]. Such a band gap allows the topological insulator to exhibit its specific properties at room temperature ($E_\mathrm{g} \gg kT$), which is very important for its potential applications.
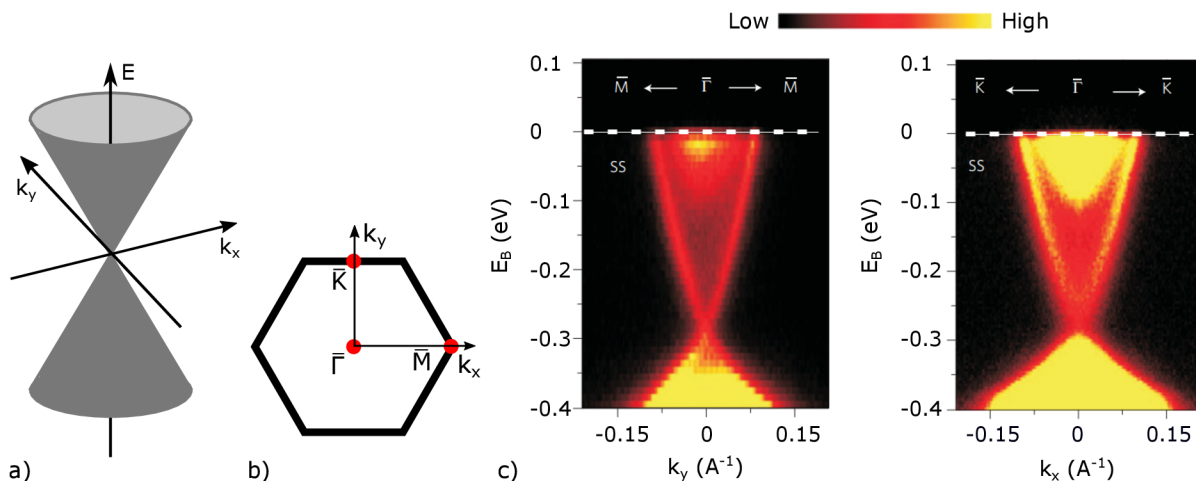

Figure 2.4: a) Schematic of a Dirac cone – linear metallic surface band. b) A schematic view of the first surface Brillouin zone of Bi_2Se_3 with a $\overline{M}$ and $\overline{K}$ points. c) High-resolution ARPES measurements of surface electronic band dispersion on Bi_2Se_3 near the $\overline{\Gamma}$-point along the $\overline{\Gamma}$–$\overline{M}$ and $\overline{\Gamma}$–$\overline{K}$ momentum-space cuts. This measurement shows a single surface band spanning across the band gap of the system. Adapted from: [13].

Although Bi_2Se_3 is currently one of the most representative examples of 3D topological insulators, there are others with similar properties. Zhang et al. [15] published a series of first-principles electronic structure calculations of stoichiometric materials Bi_2Se_3, Bi_2Te_3, Sb_2Te_3 and Sb_2Se_3 and according to their results only Sb_2Se_3 does not exhibit metallic states on the surface. All other compounds show a single Dirac cone spanning across the band gap in the center of the surface Brillouin zone. These claims were confirmed by Hsieh et al. [16] showing a ARPES measurement of Bi_2Te_3 and Sb_2Te_3, featuring the calculated surface states. These facts also explained the earlier ARPES measurement of Bi_2Te_3 showing, at the time, puzzling linear features, presented by Noh et al. [17].

2.3. Bismuth telluride

Bismuth telluride (Bi_2Te_3) is a well-known material in condensed matter physics and its exceptional thermoelectric properties are known for more than sixty years [18]. Bi_2Te_3 is currently very frequently used material in cooling devices based on Peltier effect and thermoelectric generators [19].

As Bi_2Te_3 has reappeared in 2009 as a 3D topological insulator, the interest in its properties has risen again, and many investigations have been done since that. Despite the intensive research done on this material, understanding of its bulk band structure, which is fundamental for the origin of the surface states, is still quite incomplete. Reported values of the band gap from first-principle calculations, ARPES or optical measurement

fall into a rather broad interval of $E_g = (50 - 300)$ meV. Even the nature of the band gap, whether it is direct or indirect, and its position in the Brillouin zone remains undetermined, as they differ in dependence on the method of investigation.

2.3.1. Physical properties of Bi_2Te_3

Bi_2Te_3 grows in a trigonal crystal structure with the space group $R\bar{3}m$. It is a layered material consisting of three $Te^1{-}Bi{-}Te^2{-}Bi{-}Te^1$ quintuple-layers as a fundamental building block stacked in an ABCABC sequence separated by van der Waals gaps [20]. The unit cell can be described by two equivalent sets of base vectors, either the trigonal or rhombohedral system described by black and green lines in Figure 2.5 a), respectively. The position of atoms in different layers is shown in Figures 2.5 b) and c) [15, 20]. As the polar-covalent bonds of $Bi - Te$ inside of a quintuple layer are much stronger than the van der Waals bonds of $Te^1 - Te^1$ between them, the material is easily cleavable in a direction perpendicular to the c-axis [19].
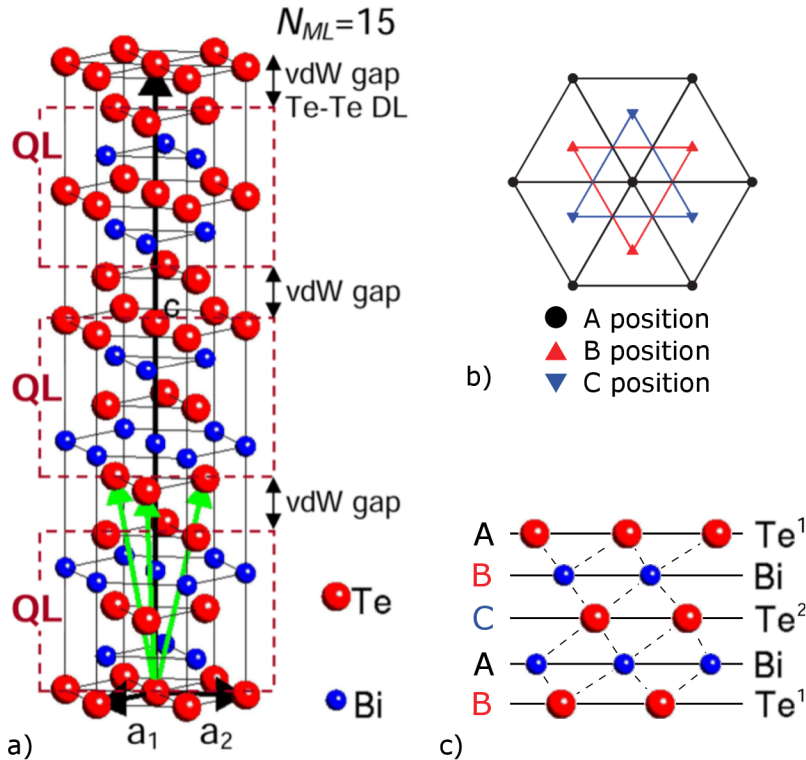

Figure 2.5: a) Unit cell of Bi_2Te_3 where black arrows are the trigonal base vectors a_1, a_2 and c (green arrows indicate an alternative definition of the crystal structure using rhombohedral base vectors) consisted of 15 layers divided to three quintuple-layers of $Te^1{-}Bi{-}Te^2{-}Bi{-}Te^1$ and bounded together by van der Waals bonds. Images taken and adapted from: [15, 20]

Thermoelectric figure of merit of Bi_2Te_3 at room temperature is the highest among all bulk materials, making Bi_2Te_3 a superior thermoelectric material for harvesting energy [20]. Most Peltier cooling devices and thermoelectric generators use alloys of Bi_2Te_3 with Sb_2Te_3 or Bi_2Se_3 (Sb_2Te_3 for p-type and Bi_2Se_3 for n-type Bi_2Te_3) as its working material [19]. It was found that the electrical and thermal conductivities are strongly anisotropic with much higher values along the quintuple-layers than across the van der Waals gaps – unlike the Seebeck coefficient that does not depend on the orientation [21].

2.3.2. Growth of thin Bi_2Te_3 layers

Most ARPES studies are performed on bulk samples of Bi_2Te_3, cleaved in an ultra-high vacuum. However, bulk materials are not suitable for practical applications and epitaxially grown thin layers are often required. To obtain epitaxial crystals of Bi_2Te_3 in pristine quality, a molecular beam epitaxy is frequently used as a method of growth. Epitaxy is a type of crystal growth where the deposited crystal layers grow with a defined crystal structure and orientation with respect to the substrate. This pre-defined crystal structure leads to crystals with fewer defects and higher quality in general. The epitaxial growth is usually achieved by decreasing the deposition rate of about 1 monolayer per second [20].

It is crucial to choose the right substrate material, which would possess a crystal lattice and thermal expansion parameter similar to the grown material because the crystal structure of the grown crystal adjusts to the substrate. When the lattices do not match, the strain does build-up gradually to the point where the growth relaxes to the natural crystal lattice, resulting in defects. For the growth of Bi_2Te_3, 111-face of BaF_2 can be used, with a lattice mismatch to Bi_2Te_3 $a/a_{\parallel} = 0.04\%$ making it practically lattice-matched. Cleaved 111-faced BaF_2 can also be almost step-free in tens of square millimeters and is highly transparent from the visible to infrared region, except for a reststrahlen band around $E = 22$ to $40\,\mathrm{meV}$ [22], making it a perfect substrate for an optical transmission measurement [20].

To achieve the epitaxial growth mode, the deposition rate must be very low. High purity material is heated in an effusion cell and evaporates (or sublimates) to create a molecular beam. For the growth of Bi_2Te_3, either combination of Bi and Te or a compound of bulk Bi_2Te_3 can be used. Controlling the temperature of evaporated material affects the flux of the molecular beam, and therefore, it is possible to precisely control the stoichiometry of the grown compound, as well as the doping by an addition of different materials. The beam of particles evaporated from the effusion cell is collimated only by an aperture between the source material and the substrate. Therefore, it is required to increase the mean free path of the particle, i.e., a mean distance a particle will travel between two collisions, to the distance between the effusion cell and the substrate. That is done by lowering the pressure inside the chamber to the ultra-high vacuum of $P = 10^{-6} - 10^{-8}$ Pa to prevent the collisions with the atmosphere gas inside of the chamber. The requirement of ultra-high vacuum is a rather strong constraint, but it also dramatically reduces the impurity level below one part in a million, which is also crucial for the preparation of high-quality crystals [23, 24].

2.3.3. Surface states

The electronic bands in Bi_2Te_3, both in bulk and on the surface, are heavily influenced by a strong spin-orbital interaction, which is one of the basic ingredients that give rise to the appearance of topological surface states.

The first experimental observation of gapless surface states in otherwise gapped Bi_2Te_3 was published by Noh at al. in 2008 [17] which makes this material one of the first discovered 3D topological insulator. It was found that the electronic band structure on the surface of Bi_2Te_3 changes significantly in time after the sample cleavage. As seen in Figure 2.6, with passing time, the valence band splits into two separate branches, its energy is lowered and new linear band with a circular Fermi surface appears spanning across the band gap after 60 minutes. The appearance of the surface states after one hour

is explained by a slow relaxation of the crystal lattice, especially the shift of the quintuple inter-layer distance [17].
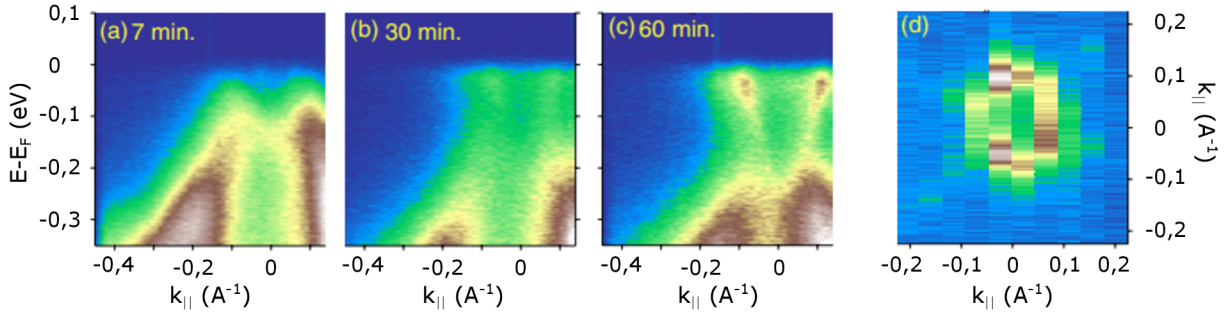

Figure 2.6: Evolution of ARPES spectra in time after cleavage of the Bi_2Te_3 sample. The elapsed time is (a) 7 minutes, (b) 30 minutes and (c) 60 minutes. (d) Constant energy map of the surface state at $E = E_F$. Taken from: [17].

Later on, in 2009, a study dedicated to the surface states in Bi_2Te_3 and similar materials was published by Hsieh at al. [16]. It was found that the surface states are well characterized by a single topological Dirac cone that evolves in about an hour after cleavage of the sample. The ARPES measurement was also complemented by first-principles calculations. It was concluded that Bi_2Te_3 is a semiconductor with an indirect spin-orbit-induced bulk band gap of $E_F \approx 150$ meV.

It was also found that the Fermi surface of the surface states (in low resolution in Figure 2.6) is not strictly circular as would be expected in a topological insulator with a Dirac cone. As seen in Figure 2.7, further from the Dirac point, the linear surface band is warped to a hexagon [25, 26].
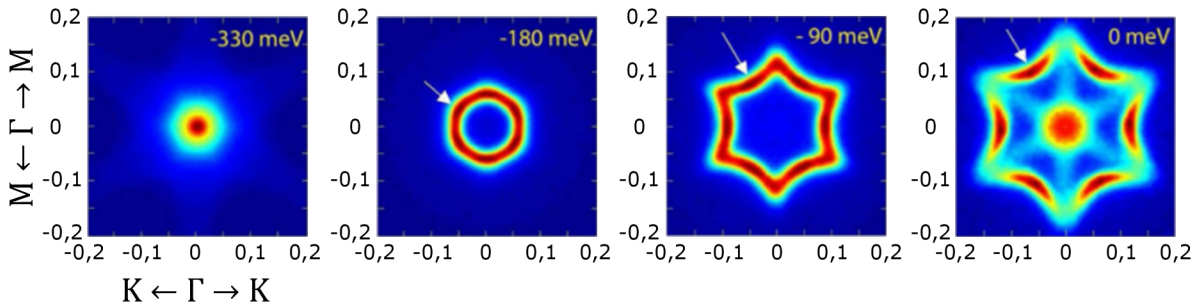
Figure 2.7: ARPES measured constant energy maps of the center of the Brillouin zone showing cuts through the warped Dirac-cone of surface states. The density of states (DOS) grows from blue (no DOS) to dark red (strong contribution to DOS). Adapted from: [26].

2.3.4. Band gap

Even though Bi_2Te_3 is a matter of intense investigations for both its unusual thermoelectric properties and more recently discovered topological properties, there are still some fundamental characteristics that the scientific community does not agree on. Perhaps, the most important are the properties of its energy band gap. Surprisingly, at the moment, there is still a dispute about a width, nature (direct versus indirect) of the band gap and even its position in the Brillouin zone (Figure 2.8 a)) as the evidence differ greatly

depending on the used method of investigation. The current consensus only implies that Bi_2Te_3 is a narrow-gap semiconductor with inverted ordering of bands around the Γ point resulting in a single band of metallic states on the surface.

Probably the most direct method of probing the band structure, angle-resolved photoemission spectroscopy, shows an indirect band gap of $E_g \approx 160\,\text{meV}$ [16, 25]. As seen in Figure 2.8 b), the band extremum of the conduction band is at the Γ point of the Brillouin zone, but at the same point, the "camelback" profile of the valence band displays a local minimum, making the band gap indirect. The ARPES studies are often complemented by first-principle calculations that usually suggest the importance of spin-orbital interaction to form an inverted gap at the Γ point [16].

However, there are significant drawbacks of ARPES technique. For one, the photoemission in ARPES is primarily sensitive to the surface of the studied sample (with the typical penetration depth around 1 nm) and brings almost no information from the bulk. As was shown by Noh et al. [17] in Figure 2.6, the surface band structure of Bi_2Te_3 differs significantly from the bulk in some time after the sample cleavage and therefore, only surface bands are observed. The second drawback of ARPES technique is that it only focuses on a small part of the Brillouin zone (usually the surroundings of the Γ point because of the surface states) and unlike e.g., electron transport measurement, it does not have any information about the rest of the Brillouin zone. Therefore, it is not possible to determine whether the observed extremum is global or just a local one.
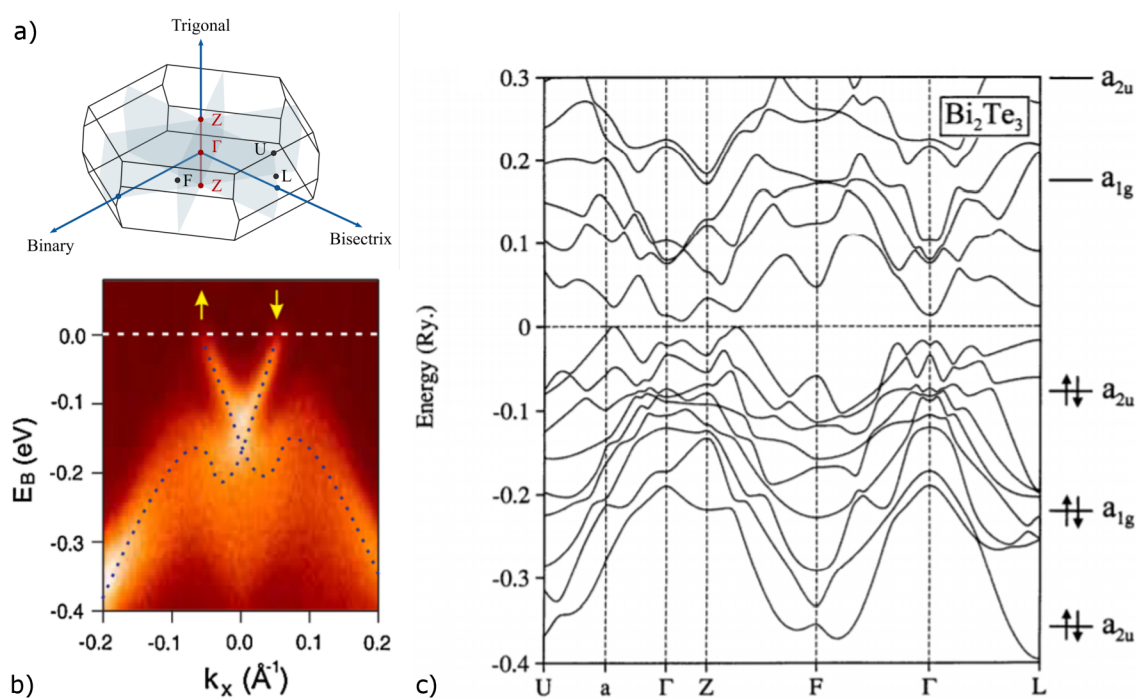
Figure 2.8: a) ARPES measurement around $\overline{\Gamma}$ point of Bi_2Te_3 with a distinctive "camelback" profile of a valence band resulting in a indirect band gap. The dashed line represents the energy of the bottom of the conduction band. Adapted from: [16] b) Calculation of a Bi_2Te_3 band structure using a density-functional theory with the spin–orbit interaction included. Adapted from: [27] c) The schematic view of the first Brillouin zone of Bi_2Te_3 with indicated mirror planes and trigonal, bisectrix and binary axes. Taken from: [1].

Most of the theoretical studies of Bi_2Te_3 do, indeed, show an indirect band gap in the center of the Brillouin zone (Figure 2.8 c)). However, they also propose a band structure

comprising six equivalent valleys for the valence band, located pairwise in the mirror planes, with non-parabolic dispersion relations and strongly anisotropic effective mass. However, the calculated positions of extrema for the conduction band differs among studies [27, 28]. Also, presumably more accurate GW calculations predict multiple extrema of the highest valence band and rather indirect band gap [29, 30]. The deduced band gap width appears to be strongly dependent on the used functional and it falls into a relatively broad range between 50 and 200 meV.

In past, models with six and twelve valleys were proposed [31]. For six valleys, the gap would be centered in one of the mirror planes or on the binary axes. Twelve valleys do appear if the gap is positioned in any other arbitrary point (except $Z-\Gamma$ line). A magneto-transport experiment that supports the model of six valleys located in the mirror planes [31] was done by H. Köhler. A series of electron transport measurements in a magnetic field and analysis of quantum oscillations for samples with varying doping was done for both n-type [32] and p-type [33] Bi_2Te_3 samples. It was found that the results correspond well to the six-valley model with ellipsoidal Fermi surfaces. In addition, fairly similar values of effective masses of electrons and holes were found ($m^*_{val} = 0.08m_e$ and $m^*_{con} = 0.06m_e$, where m_e is a mass of an electron).

3. Optical response of solid-state matter in external magnetic field

Landau level spectroscopy is a method of choice to study the band structure of solids. This method follows the changes in the optical response that are induced by the externally applied magnetic field, which is sufficiently strong to quantize electronic states into Landau levels. The analysis of the observed inter-Landau level excitations often helps to reconstruct the electronic band structure with the precision significantly higher as compared to, e.g., ARPES technique. In this way, we may learn, for instance, about the width and nature of the band gap or determine other band structure parameters such as masses of charge carriers, their velocities, g factors or the degree of anisotropy.

3.1. Optical response of solids

The optical properties of any solid are encoded in the specific complex response functions. The index of refraction $N(\omega)$, dielectric function $\varepsilon(\omega)$ and optical (dynamical) conductivity $\sigma(\omega)$ belong to the most used ones.

The complex index of refraction (or sometimes refractive index) N is composed of the real and imaginary parts:

$$N = n + ik, \tag{3.1}$$

where the real part n is usually also reffed to as an index of refraction, imaginary part k is called an extinction coefficient and i is the imaginary unit. The index of refraction (its real part) n of dielectric material is linked to a speed of light v inside of the material as $v = = c/n$, where c is the speed of light in vacuum. The extinction coefficient k describes the decrease of an intensity of radiation passing through the material with $\propto \exp\left[-(4\pi k/\lambda_0)d\right]$, where λ_0 is a wavelength of the radiation in a vacuum and d is a distance the radiation travels. The argument of the exponential function is usually noted as $-\alpha d$, where α is called an absorption coefficient. Distance from the surface, where $\alpha d = 1$ and the intensity drops to $1/e \approx 37$ %, is called a penetration depth [34].

In general, a dielectric function is a second-order tensor but in an isotropic material, it takes a form of a scalar function that only depends on an angular frequency ω, defined by one of the constitutive relations as:

$$\boldsymbol{D} = \varepsilon_0 \varepsilon(\omega) \boldsymbol{E}, \tag{3.2}$$

3. OPTICAL RESPONSE OF SOLID-STATE MATTER IN EXTERNAL MAGNETIC FIELD

where $\boldsymbol{D}$ is an electric displacement field, ε_0 is the permittivity of vacuum and $\boldsymbol{E}$ is an intensity of an electric field. The dielectric function ε and index of refraction N are equivalent with a relation:

$$\varepsilon(\omega) = N^2. \tag{3.3}$$

The angular frequency ω is often transferred to other quantities such as the frequency f, wavelength λ, wavenumber $\tilde{\nu}$ or energy (usually in electronvolts or millielectronvolts) using relations:

$$\omega = 2\pi f = 2\pi \frac{c}{\lambda} = 2\pi c\tilde{\nu} = \frac{eE\,[\text{eV}]}{\hbar}, \tag{3.4}$$

where c is the speed of light in vacuum, e is en elemental charge and $\hbar$ is reduced Planck constant.

Same as the index of refraction, the dielectric function is a complex quantity, with the real and imaginary parts, both dependent on the frequency of radiation:

$$\varepsilon(\omega) = \varepsilon_1(\omega) + i\varepsilon_2(\omega), \tag{3.5}$$

where $\varepsilon_1(\omega)$ and $\varepsilon_2(\omega)$ are real and imaginary part of dielectric function, respectively. The real part $\varepsilon_1(\omega)$ describes how the electric field distorts the distribution of charge in the material and the imaginary part $\varepsilon_2(\omega)$, similarly to the extinction coefficient k, describes its absorption properties.

Finally, in some cases, instead of the dielectric function $\varepsilon(\omega)$ optical conductivity $\sigma(\omega)$ is used. Optical conductivity is in isotropic materials defined as a proportionality factor between the intensity of electric field $\boldsymbol{E}$ and induced current density $\boldsymbol{j}$:

$$\boldsymbol{j}(\omega) = \sigma(\omega)\boldsymbol{E}(\omega). \tag{3.6}$$

From Maxwell equations, the relationship between $\varepsilon(\omega)$ and $\sigma(\omega)$ can be derived as:

$$\sigma(\omega) = \sigma_1(\omega) + i\sigma_2(\omega) = -i(\omega)\varepsilon_0(\varepsilon(\omega) - 1), \tag{3.7}$$

resulting in the real and imaginary parts of optical conductivity:

$$\sigma_1(\omega) = \omega\varepsilon_0\varepsilon_2(\omega) \quad \text{and} \quad \sigma_2(\omega) = -\omega\varepsilon_0(\varepsilon_1(\omega) - 1). \tag{3.8}$$

Later on, when presenting the results of our optical experiments at $B = 0$, the optical conductivity, namely its real part, will be used to describe the dissipative part of the optical response of Bi_2Te_3, mainly due to interband excitations.

As the electron excitations in non-conducting materials may only occur between two bands across the band gap (interband transitions), their contribution to the real part of optical conductivity $\sigma_1(\omega)$, below the energy of band gap E_g is, in an ideal case, zero. For energies above the band gap, the onset of absorption, known as fundamental absorption edge, occurs. The strength of the absorption edge depends on the relative positions of valence and conducting bands in the Brillouin zone. Materials where the valence and conduction bands extrema occupy the same wavevector, display a strong absorption edge and are said to be direct. Conversely, materials where valence and conduction bands extrema are located further from each other, are referred to as systems with an indirect energy band gap. These systems generally have much weaker absorption edge as electrons also need an interaction with phonon to be promoted to the other band [2]. In conducting materials, electronic excitations at energies well below the (possibly present) band gap appear. These are related to the response of free electrons, and most often, they are described using the classical model of Drude.

3.2. Formation of Landau levels in a conventional materials

To illustrate the impact of the externally applied magnetic field on the optical response of a solid, let us start with the simplest case of a three-dimensional free electron in the magnetic field.

Let us assume a free electron (an electron within a gas of non-interacting particles) in a homogeneous magnetic field $\boldsymbol{B}$, described by vector potential $\boldsymbol{A}$. To find corresponding eigenstates and eigenvalues, we search for solution of the Schrödinger equation:

$$i\hbar\frac{\partial\Psi(x,y,z,t)}{\partial t} = \hat{H}\Psi(x,y,z,t). \tag{3.9}$$

Since the applied magnetic field is constant in time, we may only solve the time-independent Schrödinger equation, which is equivalent to searching for eigenvectors and eigenvalues of the Hamiltonian:

$$\hat{H}\psi(x,y,z) = E\psi(x,y,z), \tag{3.10}$$

where $\hat{H}$ is the Hamiltonian, an operator corresponding to the sum of kinetic and potential energy of the particle, $\psi(x,y,z)$ is the wavefunction dependent on x, y and z space coordinates and E stands for energy. The Hamiltonian for an electron in the homogeneous magnetic field, described by the vector potential $\boldsymbol{A}$, reads:

$$\hat{H} = \frac{1}{2m_\mathrm{e}}(\boldsymbol{p} - q\boldsymbol{A})^2, \tag{3.11}$$

where m_e is a free-electron mass, $\boldsymbol{p}$ is its vector of momentum and q is electric charge.

To solve the Schrödinger equation, the standard asymmetric Landau gauge is adopted, in which the vector potential $\boldsymbol{A} = (-By, 0, 0)$ corresponds to the magnetic field applied along the z direction $\boldsymbol{B} = (0, 0, B)$. After implementing the Landau gauge we can write the equation (3.10) as:

$$\frac{1}{2m_\mathrm{e}}\left((p_\mathrm{x} - eBy)^2 + p_\mathrm{y}^2 + p_\mathrm{z}^2\right)\psi(x,y,z) = E\psi(x,y,z). \tag{3.12}$$

Since the equation does not depend on either x or z, the $\left[\hat{H},\hat{p}_\mathrm{x}\right] = \left[\hat{H},\hat{p}_\mathrm{z}\right] = 0$ and the wavefunction $\psi(x,y,z)$ can be separated as $\psi(x,y,z) = X(x)Y(y)Z(z) = e^{-i(k_\mathrm{x}x + k_\mathrm{z}z)}X(y)$ and the previous equation can be rewritten as:

$$\left[\frac{1}{2}m_\mathrm{e}\frac{e^2B^2}{m_\mathrm{e}^2}\left(y - \frac{p_\mathrm{x}}{eB}\right)^2 + \frac{p_\mathrm{y}^2}{2m_\mathrm{e}}\right]Y(y) = \left(E - \frac{p_\mathrm{z}^2}{2m_\mathrm{e}}\right)Y(y), \tag{3.13}$$

where one can recognise the equation describing one-dimensional quantum harmonic oscillator:

$$\left[\frac{1}{2}m_\mathrm{e}\omega^2\left(y - y_0\right)^2 + \frac{p_\mathrm{y}^2}{2m_\mathrm{e}}\right]Y(y) = \varepsilon Y(y), \tag{3.14}$$

with a frequency ω, center of the oscillations y_0 and energy ε:

$$\omega = \frac{eB}{m_\mathrm{e}} \quad , \quad y_0 = \frac{p_\mathrm{x}}{eB} \quad \text{and} \quad \varepsilon = \left(E - \frac{p_\mathrm{z}^2}{2m_\mathrm{e}}\right). \tag{3.15}$$

As ω is identical to a classical cyclotron frequency of an orbital motion of a charged particle in a magnetic field, we will denote it as ω_c.

The energy levels of such an oscillator still have parabolic dispersion in the z direction, which corresponds to the free motion along the direction of the applied magnetic field, but the motion perpendicular to B becomes quantized, the kinetic energy can only reach discrete, equidistantly spaced values, so-called Landau levels:

$$E_n = \hbar\omega_c \left(n + \frac{1}{2} \right) + \frac{k_z^2 \hbar^2}{2m_e}. \tag{3.16}$$

Finally, the Landau level spectrum in a region, where the electronic band is approximately parabolic, is then:

$$E_{LL,n} = \frac{eB}{m_e}\hbar \left(n + \frac{1}{2} \right) + \frac{k_z^2 \hbar^2}{2m_e}. \tag{3.17}$$

As seen in Figure 3.1, the Landau level spectrum of an electron in a parabolic band is equidistant and the adjacent levels are separated by the energy given by the classical cyclotron frequency $\frac{eB}{m_e}$.
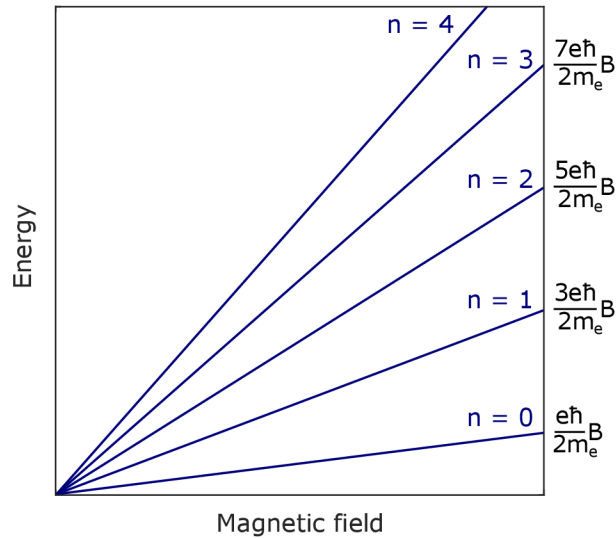

Figure 3.1: Plot of the lowest five Landau levels of electrons in band with a parabolic dispersion. The adjacent levels are separated by cyclotron energy defined by classical cyclotron frequency $\omega_c = eB/m$ of an free electron in a magnetic field.

3.3. Two-band model of Dirac massive electrons

The previous section deals with a free electron and a single parabolic band. In reality, to explain a response of electrons in a material, more complex models, comprising of two or more bands, have to be proposed.

It this thesis, we adopt a two-band model of Dirac massive electrons to describe a magneto-optical response of Bi_2Te_3. This two-band model describes a time-reversal-invariant direct-gap semiconductor with an isotropic electronic band structure [35, 36].

It implies only two free parameters, half gap Δ and band edge velocity v_D. The corresponding Hamiltonian may be derived, *e.g.*, using the first-order $\mathbf{k} \cdot \mathbf{p}$ theory applied at a particular point, $\mathbf{k_0}$, of the Brillouin zone:

$$\hat{H} = \begin{pmatrix} \Delta & \hbar v_D(q_x + iq_y) \\ \hbar v_D(q_x - iq_y) & -\Delta \end{pmatrix}, \tag{3.18}$$

where $\mathbf{q} = \mathbf{k} - \mathbf{k_0} = (q_x, q_y, 0)$. The Hamiltonian describing electrons and holes with an opposite spin projection in the twice degenerate bands is obtained by the complex conjugation of $\hat{H}$ ($\hat{H}^*$). Notably, only vanishing q_z momenta are considered because the $q_z = 0$ states dominate the overall optical response when the magnetic field is applied along the z axis.

The Hamiltonian (3.18) gives rise to the conduction and valence bands with a characteristic relativistic-like hyperbolic profile: $E(k) = \pm\sqrt{\Delta^2 + \hbar^2 v_D^2 k^2}$. They are separated by the band gap of 2Δ and display the full electron-hole symmetry. For large momenta, the dispersion of charge carriers approaches the ultra-relativistic limit, $E(\mathbf{k}) \approx \pm\hbar v_D|\mathbf{k}|$. This allows us to treat the v_D parameter, which describes the coupling between bands, as the effective velocity of light in the explored system.

Usually, more complicated form of Dirac massive electrons model is considered e.g., a four-band model with additional parameters like particle-hole asymmetry and band inversion included. However, for simplicity, here, the most elementary form of the model is assumed, and as will be shown in the experimental section, that for a description of Landau levels of Bi_2Te_3 it is fully sufficient.

3.3.1. Landau levels in a model of Dirac massive electrons

To find the Landau level spectrum, of a Dirac system, the time-independent Schrödinger equation is solved. After introduction of magnetic field and Landau gauge, the Hamiltonian (3.18) can we rewritten as:

$$\hat{H} = \begin{pmatrix} \Delta & v_D((p_x - eBy) + ip_y) \\ v_D((p_x - eBy) - ip_y) & -\Delta \end{pmatrix}, \tag{3.19}$$

and the Schrödinger equation for a two-component wavefunction takes form of:

$$\begin{pmatrix} \Delta & v_D((p_x - eBy) + ip_y) \\ v_D((p_x - eBy) - ip_y) & -\Delta \end{pmatrix} \begin{pmatrix} \Phi_A \\ \Phi_B \end{pmatrix} = E \begin{pmatrix} \Phi_A \\ \Phi_B \end{pmatrix}. \tag{3.20}$$

From equation (3.20) it is possible to get two coupled equations for the wavefunctions Φ_A and Φ_B:

$$v_D (p_x - eBy + ip_y) \Phi_B = (E - \Delta)\Phi_A \tag{3.21}$$

$$v_D (p_x - eBy - ip_y) \Phi_A = (E + \Delta)\Phi_B. \tag{3.22}$$

After decoupling the equations and multiplying both sides with $1/(2m_e)$, where m_e is an electron mass, the equations are again identical to a one dimensional quantum harmonic oscillator:

$$\frac{1}{2m_e}\left((p_x - eBy)^2 + p_y^2\right)\Phi_A = \frac{1}{2m_e}\left(\frac{(E^2 - \Delta^2)}{v_D^2} + \hbar eB\right)\Phi_A = \varepsilon\Phi_A \tag{3.23}$$

with allowed energy states:

$$\varepsilon = \frac{1}{2m_\mathrm{e}}\left(\frac{(E^2 - \Delta^2)}{v_\mathrm{D}^2} + \hbar e B\right) = \frac{eB}{m_\mathrm{e}}\hbar\left(n + \frac{1}{2}\right). \tag{3.24}$$

From equation (3.24) an energy spectrum of Landau levels can be derived:

$$E_{\mathrm{LL},n} = \pm\sqrt{\Delta^2 + 2e\hbar v_\mathrm{D}^2 n B}, \tag{3.25}$$

where $n > 0$. In addition, there exists a pair of spin-polarized zero-mode Landau levels
($n = 0$) with the energies $E_0 = \Delta$ and $E_0 = -\Delta$, which correspond to the $\hat{H}$ and $\hat{H}^*$
Hamiltonians, respectively.

It is important to notice that as shown in Figure 3.2, Landau levels in non-parabolic
bands are no longer equidistant and their dispersion with the magnetic field is not linear.
When the parameter Δ reaches zero, and the system is gapless, the characteristic square-
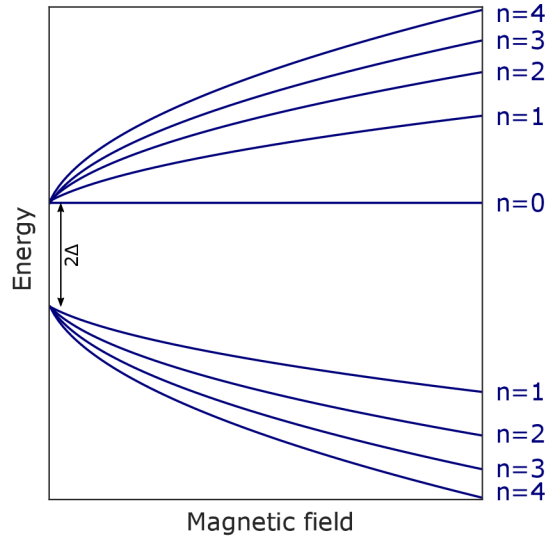root shape of the Landau levels emerges e.g., in a case of graphene [37].

Figure 3.2: Plot of Landau levels of electrons in a linear band, corresponding to the Hamilto-
nian $\hat{H}$. The pronounced non-linearity of Landau levels is characteristic for such
a systems as well as the decreasing distance of adjacent levels with increasing
Landau level index n.

3.4. Inter-Landau level transitions

To explain the optical response of a material in a magnetic field we need both, Landau
level spectrum of a given system and the selection rules for allowed inter-Landau level
transitions.

As the electric dipole perturbation, an uniform oscillating electric field $\boldsymbol{E}$ of inten-
sity E_0 is applied perpendicular to the z-axis. The electric field is described by a vector
potential $\boldsymbol{A}$:

$$A_x = \frac{E_0}{i\omega}e^{-i\omega t} + \text{c.c.}, \quad A_y = A_z = 0, \tag{3.26}$$

where c.c. stands for complex conjugate, that gives rise to the stimulated emission, but in this work will not be discussed further [2, 38].

Such a vector potential corresponds to electric field via $\boldsymbol{E} = -\partial \boldsymbol{A}/\partial t$:

$$E_x = E_0 e^{-i(\omega t)}, \tag{3.27}$$

Inserting the vector potential (3.26) into Hamiltonian (3.11), we obtain:

$$\hat{H} = \frac{1}{2m}\left[\boldsymbol{p} + e\left(\boldsymbol{A}\right)\right]^2 = \tag{3.28}$$

$$\approx \frac{1}{2m}\left(\boldsymbol{p}^2 + e\boldsymbol{p}\cdot\boldsymbol{A} + e\boldsymbol{A}\cdot\boldsymbol{p}\right)^2 + e^2\boldsymbol{A}^2. \tag{3.29}$$

Using a definition of $\boldsymbol{p} = -i\hbar\nabla$, the term $(\boldsymbol{p}\cdot\boldsymbol{A})$ can be expressed as:

$$(\boldsymbol{p}\cdot\boldsymbol{A})f(r) = A\cdot(-i\hbar\nabla f) + (-i\hbar\nabla\cdot A)f. \tag{3.30}$$

As $\nabla\cdot A = 0$, it is also true that $\boldsymbol{p}\cdot\boldsymbol{A} = \boldsymbol{A}\cdot\boldsymbol{p}$. Also, the term $e^2\boldsymbol{A}^2$ is neglected as we are interested in the linear response only. The Hamiltonian (3.28) than may we rewritten as:

$$\hat{H} = \frac{1}{2m}p^2 + \frac{e}{m}\boldsymbol{A}\cdot\boldsymbol{p} = \tag{3.31}$$

$$= \hat{H}_0 + \hat{H}'. \tag{3.32}$$

Additionally to the original unperturbed Hamiltonian $\hat{H}_0$, the extra term $(e/m)\boldsymbol{A}\cdot\boldsymbol{p}$ is called a monochromatic perturbation Hamiltonian $\hat{H}'$ and it describes the interaction between the radiation and the Bloch electrons [2].

In general, for relatively weak perturbing fields, the rate at which electrons are promoted, via the external radiation, from the initial state i to the final state f, is given by the Fermi golden rule:

$$W_{\text{if}} = \frac{2\pi}{\hbar}\left|M\right|^2\delta(E_{\text{f}} - E_{\text{i}} \pm \hbar\omega), \tag{3.33}$$

where M is a matrix element in a form of $|\langle f|H'|i\rangle|^2$ and the $\pm\hbar\omega$ terms in the delta function corresponds to the photon emission and absorption, respectively.

Let us investigate the matrix element a little further. It is possible to express the Bloch functions as:
$$|i\rangle = u_v f_i \quad |f\rangle = u_c f_f, \tag{3.34}$$

where u_v, u_c are Bloch functions at $k = 0$ and f_i, f_f are envelope functions [39]. The matrix element can be rewritten as:

$$\langle f|\boldsymbol{A}\cdot\boldsymbol{p}|i\rangle = A\int u_c^* f_f^*\boldsymbol{p}u_v f_i dr = \tag{3.35}$$

$$= A\int u_c^* f_f^*(u_v\boldsymbol{p}f_i + f_i\boldsymbol{p}u_v)dr = \tag{3.36}$$

$$= A\left(\int u_c^*\boldsymbol{p}u_v f_f^* f_i dr + \int u_c^* u_v f_f^*\boldsymbol{p}f_i dr\right). \tag{3.37}$$

Since the indexes c,v represent the band index, excitations inside of a single band are characterized by a condition $c = v$, where only the second term of the equation (3.37)

is non-zero. This term may, therefore, be labeled as an intraband term. On the other hand, when $c \neq v$, the intraband term is zero, and only the first term of the equation (3.37) contributes to absorption. In this case, indexes c and v denote the conduction and valence bands, respectively, and therefore, the matrix element describes promotions of electrons between them [39].

Generally, the transitions for which the matrix element is non-zero are referred to as optically allowed or active. The transitions with matrix elements independent of the wave vector of light are called electric-dipole active transitions and usually dominate the optical response of Landau-quantized systems over other, in the integral intensity weaker lines, such as electric-quadrupole, octupole, but also magnetic-dipole active transitions. In this thesis, we will only consider transitions that are electric-dipole active.

A closer analysis of the matrix elements implies that electric-dipole transitions in isotropic systems follow the selection rule: $n \to n \pm 1$, where the $n \to n+1$ and $n \to n-1$ corresponds to absorption (but also emission) of a photon with either left or right circular polarization. In systems that lack the isotropy, or better to say, full rotation symmetry along the direction of the applied magnetic field, the selection rules become more complex as will be discussed in the context of our results on Bi_2Te_3.

Also, the selection rules mentioned above are derived for the Faraday configuration (Figure 3.3), where the incident radiation is parallel to the applied magnetic field. In a Voigt configuration, however, the incident radiation is perpendicular to the magnetic field. In this configuration, an electric field component of the radiation can be either perpendicular or parallel to the magnetic field, depending on the direction of its polarization. When the electric field component is polarized perpendicular to the magnetic field, the same selection rules, as in the Faraday configuration apply, however, when the polarization is parallel to the magnetic field, different sets of allowed transitions occur. The non-zero $\boldsymbol{E}$ component in the direction of the magnetic field does forbid the $n \to n \pm 1$ transitions, but simultaneously allows the $n \to n$ transitions [40].
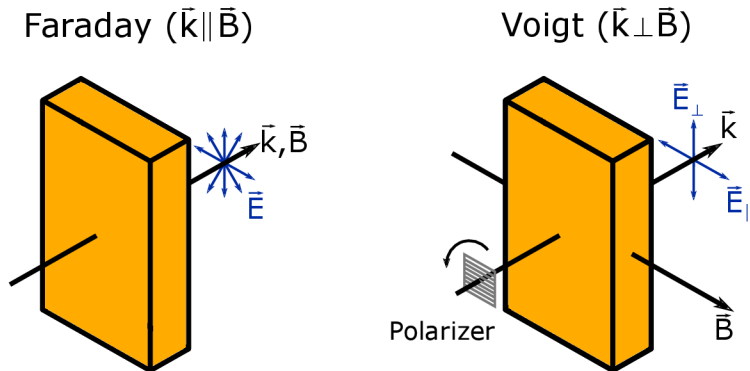

Figure 3.3: Experimental setup for Faraday ($\boldsymbol{k} \parallel \boldsymbol{B}$), where $\boldsymbol{B}$ is always perpendicular to $\boldsymbol{E}$ and Voigt ($\boldsymbol{k} \perp \boldsymbol{B}$) configurations. In the Voigt configuration the optical response depends on a polarization of the incident radiation, as $\boldsymbol{E}$ may be both, parallel and perpendicular to $\boldsymbol{B}$, depending on the orientation of the polarizer.

A theoretical study dealing with selection rules for Dirac massive fermions was presented by O. Ly and D. M. Basko [38]. A shifted indexing, defined as $\tilde{n} = n - \lambda\sigma/2 - 1/2$ is introduced, where $\lambda = -1$ for valence band, $\lambda = 1$ for conduction band and $\sigma = \pm 1$ corresponds to the spin of the electron. In this shifted indexing selection rules for electric-dipole intraband transitions are $\tilde{n} \to \tilde{n} \pm 1$, for both $\sigma = \pm 1$. This selection rule translates into $n \to n \pm 1$, of previously proposed indexes. For interband transitions, dominant

electric-dipole $\tilde{n} \to \tilde{n}$ transitions are accompanied with weaker $\tilde{n} \to \tilde{n} \pm 2$ transitions. For $\sigma = 1$, the $\tilde{n} \to \tilde{n}$ translates into $n \to n+1$ and $\tilde{n} \to \tilde{n}-2$ is equivalent to $n \to n-1$. For electrons with opposite spin, $\sigma = -1$, the selection rules are $n \to n-1$ for dominant transitions and $n \to n+1$ for the weaker ones. Therefore, the general selection rule $n = n \pm 1$ still holds for both intraband and interband transitions, even for the non-parabolic bands corresponding to the Hamiltonian (3.18).

This selection rule, however, applies for a band gap, with a full rotational symmetry. It was previously observed in a study of graphite [41], that other sets of selection rules may emerge when the bands are warped and lose their rotational symmetry. After analysis of higher-order in k terms, corresponding to trigonal warping of Bi_2Te_3 bands, that are not included in Hamiltonian (3.18), it was shown that additional selection rules are allowed, following: $n \to n \pm$ mod 3 [38]. After a discussion with D. M. Basko, it was established that with further lowering of the symmetry below trigonal one, additional $n \to n$ excitations might also appear in the optical response. An overview of transitions allowed by different selection rules is in Figure 3.4.
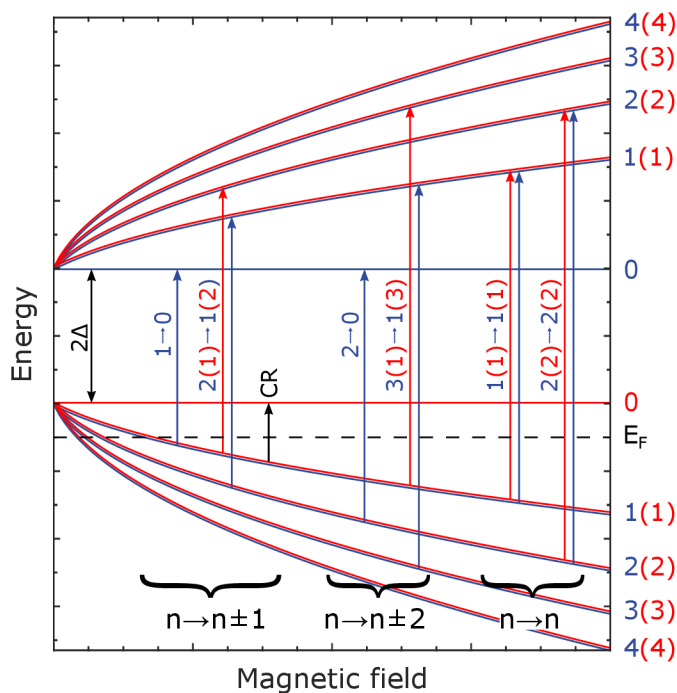
Figure 3.4: Landau levels of a Dirac system for a Hamiltonian $\hat{H}$ (blue lines) and $\hat{H}^*$ (red lines). The black dashed lines represent the value of Fermi level for a p-doped sample. Three different selection rules $L_n \to L_{n\pm1}$, $L_n \to L_{n\pm2}$ and $L_n \to L_n$, are displayed, resulting from the lowered symmetry of the originally fully rotational system.

3. OPTICAL RESPONSE OF SOLID-STATE MATTER IN EXTERNAL MAGNETIC FIELD

4. Infrared spectroscopy

An infrared range refers to a relatively broad interval of energies of $E = 1 - 1000$ meV between the visible light and microwaves. The energies of a large number of different excitations like phonons, plasmons, magnons, excitations of conduction electrons, and for narrow gap semiconductors and semimetals, even excitations across its band gap fall into this range. Therefore, it is possible to observe and study all of these phenomena using a single technique, infrared spectroscopy.

Nowadays, Fourier-transform technique is, by far, the most often applied experimental method in infrared spectroscopy and magneto-spectroscopy. This technique allows us to probe the optical response of solids using polychromatic sources of radiation. The result of Fourier-transform spectroscopy is an interferogram (dependence of intensity on the retardation), that can be converted to the wavelength-dependent signal via Fouriertransform, hence the name Fourier-transform infrared spectroscopy (FTIR). Nowadays, the Fourier transform is done almost exclusively via Fast Fourier transform algorithm as it dramatically reduces the number of necessary computations, and therefore, also required computational time.

Main advantages of FTIR over grating infrared spectrometers are a capability to measure spectral information from a broad range of wavelengths at the same time (Fellgett's advantage), and higher optical throughput as the grating monochromator in the gratings spectrometers significantly reduces the intensity of the source radiation resulting in much higher signal-to-noise ratio (Jacquinot's Advantage). These advantages are reduced by higher demands on the detector, which is usually less efficient than in the grating spectrometers, but overall the FTIR technique is much faster and, therefore, usually preferred in most laboratories [42].

4.1. Fourier-transform infrared spectrometer

The heart of the FTIR spectrometer is the interferometer. Many different types of interferometers may be used, but to this day, one of the simplest, the Michelson interferometer [43], is most commonly found in Fourier-transform infrared spectrometers. As depicted in Figure 4.1, the beam of radiation from the source is divided on the beamsplitter to one fixed and one movable plane mirror, creating a difference in phase of the separated beams, before recombining them again. If the path length is the same, the interference is constructive for all the wavelengths. If the path is different (this difference is double of the mirror position change and is called retardation δ) constructive interference will occur only for those wavelengths where retardation is integer multiple of the wavelength, and destructive interference will happen for wavelengths where retardation is an integer multiple of wavelength plus a half. As the moving mirror oscillates, the phase difference, dependent on the position of the mirror changes and radiation of different wavelengths,
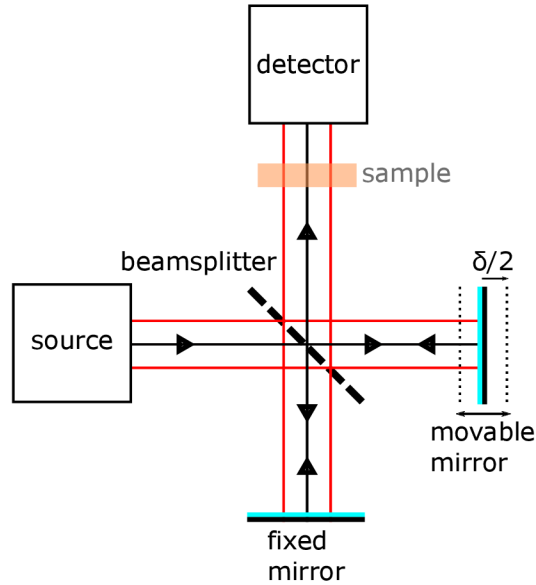
4. INFRARED SPECTROSCOPY

Figure 4.1: Schematics of Michelson interferometer showing how the source beam is divided into two paths, reflected and recombined again with a phase difference dependent on a retardation δ.

will pass the interferometer. The detector captures an interferogram, an intensity of radiation, as a function of the position of the mirror. The spectrum is then acquired by the Fourier transform of the interferogram [44].

4.1.1. Interferogram to signal

To show how does the Fourier transform of interferogram results in a spectrum, let us follow the beams in the interferometer and calculate the intensity at the detector. First, let us assume the monochromatic beam coming from the source with wavelength λ, complex amplitude A_0 and intensity $I_0 = |A_0|^2$. After passing/reflecting on the beamsplitter the respective complex amplitudes are modified as $A_r = rA_0$ and $A_t = tA_0$, where r and t are the coefficients of reflectivity and transmission of the beamsplitter. In the configuration in Figure 4.1, due to the different path length the transmitted beam gains a phase shift of $e^{i2\pi\tilde{\nu}\delta}$, where $\tilde{\nu}$ is a wavenumber of the beam, defined as $\tilde{\nu} = 1/\lambda$, and δ is a retardation of the path. After reflection at the mirror the beams pass the beamsplitter again and their complex amplitudes are once more modified as $A_r = trA_0$ and $A_t = rtA_0e^{i2\pi\tilde{\nu}\delta}$ and both beams interfere. We can then add their complex amplitudes and calculate the intensity captured by the detector as:

$$I = |A_r + A_t|^2 = (trA_0 + rtA_0e^{i2\pi\tilde{\nu}\delta})(trA_0 + rtA_0e^{-i2\pi\tilde{\nu}\delta}) \tag{4.1}$$

$$I(\delta) = 2(rt)^2 I_0 \Big(1 + \cos{(2\pi\tilde{\nu}\delta)}\Big). \tag{4.2}$$

Terms I_0 and r, t are parameters of the radiation source and the beamsplitter. In reality, they are strongly spectral dependent. Additionally, also the detector has a spectrally dependent response as every detector has varying sensitivity for different wavelengths. For simplicity, let us combine all of these spectral parameters into one, $G(\tilde{\nu})$.

It is apparent from equation (4.2) that the captured signal consists of constant and modulated components. Only the modulated component is important and is referred to as the interferogram.

24

Finally, as the infrared radiations sources have a broad spectrum, the final interferogram is a sum of all the monochromatic interferograms, but as the spectrum is continuous rather than discrete, the final response is obtained via integration over the whole spectral range:

$$I(\delta) = \int_{-\infty}^{\infty} G(\tilde{\nu}) \cos{(2\pi\tilde{\nu}\delta)}d\tilde{\nu}. \tag{4.3}$$

Such an equation is identical to the mathematical formulation of the Fourier transform and it is possible to use the inverse-Fourier transform to get the spectrum:

$$G(\tilde{\nu}) = \int_{-\infty}^{\infty} I(\delta) \cos{(2\pi\tilde{\nu}\delta)}d\delta. \tag{4.4}$$

An example of interferogram captured for transmission measurement of Bi_2Te_3 and its Fourier transform to spectrum is shown in Figure 4.2.

The term $G(\tilde{\nu})$ was introduced to cover all parameters with some spectral dependence. It contains information about the instrument (a source, a beamsplitter, a detector), but also the optical response of the possible studied sample. To separate these components, the measured sample spectra are usually normalized by the reference spectrum. That may be an empty hole or a substrate in the transmission configuration, and a gold mirror or gold coating layer when reflectivity is measured. In the experimental section, we will often use normalization by the zero-field response. That will allow us to follow the changes in the optical properties of the studied sample induced by the magnetic field.
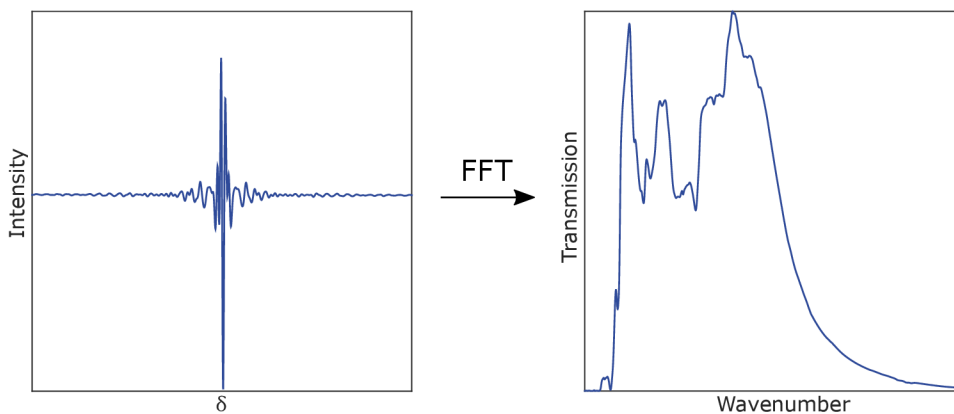

Figure 4.2: Fourier transform of captured interferogram to transmission signal.

The equation (4.4) implies integration over retardation δ from $-\infty$ to ∞, nevertheless, in reality, it is not possible to measure the interferogram in such an interval of retardation. It can be shown that the maximum of retardation $\delta_{\max}$ is related to the resolution of the spectrum as:

$$(\Delta\tilde{\nu}) \approx (\delta_{\max})^{-1}, \tag{4.5}$$

where $\Delta\tilde{\nu}$ is wavenumber difference of two closest distinguishable points [42]. The most used resolution in this thesis is $4\,\mathrm{cm}^{-1}$. To achieve this resolution, the maximum deviation of the movable mirror is $\approx 1/8$ cm. The process of further decreasing the intensity of the parts of interferogram far from its center is called apodization. It is done by multiplying

the interferogram with an even function with a maximum in its center and decreasing intensity away from it (e.g., triangular or cosine function). The intensity of the center of the interferogram is increased relative to the rest. This process reduces noise in the spectrum, but heavy apodization may also distort its shape, especially the width and intensity of relatively broad peaks [42].

Many elements affect the intensity of the measured spectrum. Some are spectral dependent as the source, beamsplitter, and detector, and have to be chosen according to the investigated spectral range, and some depend on the settings of the measurement like the scanning frequency of the interferogram and number of scans integrated into the final spectrum. In the next part, a few examples of these optical elements are briefly described.

4.1.2. Sources

In the middle infrared region, a heated rod of silicon carbide (SiC) (trade name: Globar$^{\text{TM}}$) is used as a source of the infrared radiation for its relatively broad emission spectrum with high intensity (Figure 4.3). The Globar is heated to $T = (1000 - 2000)°C$ by electrical current, and it approximately behaves as a black body radiator and emits a spectrum with a dependence on the wavenumber ν and temperature T:

$$B(\tilde{\nu},T) = 2hc^2\tilde{\nu}^3 \left(e^{\frac{hc\tilde{\nu}}{k_BT}} - 1\right)^{-1},\qquad(4.6)$$

where h is Planck constant, c is the speed of light and k_{B} is Boltzman constant.

The main disadvantage of the thermal source is the decreasing intensity of emitted radiation at low energies. According to Stefan–Boltzmann law, the black-body radiant emittance increases with $\propto T^4$, but simultaneously, the Wien's displacement law states that the peak of black-body radiation shifts to smaller wavelengths (higher energies) with increasing temperature as $\lambda_{\text{max}} \propto 1/T$. Therefore, such sources are not suitable for measurements in low energies, e.g., a far infrared range.
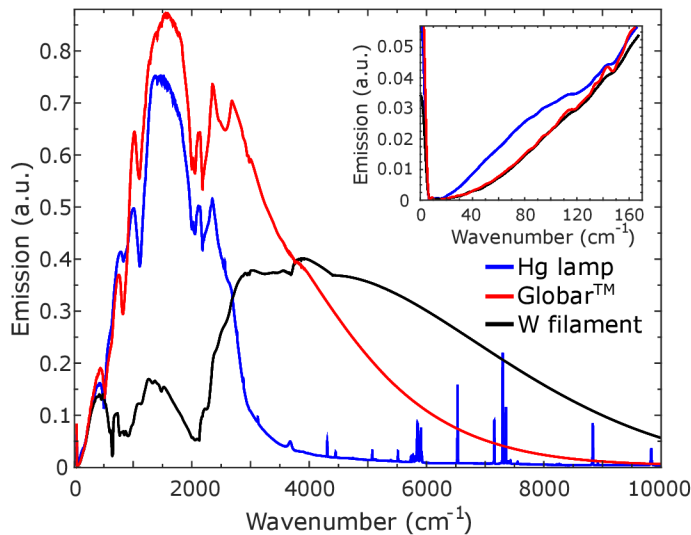
Figure 4.3: Spectral emission of different sources used in a FTIR spectrometer with a RT-DLaTGS detector. The insert shows a far infrared range with a Hg lamp showing superior signal under $\tilde{\nu} \approx 100$ cm^{-1} making it preferred choice for measuring of the low energy transitions such as cyclotron resonance.

To enhance the signal in the far infrared range, it is possible to use a Hg lamp. Even though the majority of spectral emission occurs in the visible and UV spectral range,

there is also a well-defined emission peak in the far infrared spectral range (Figure 4.3). As a matter of fact, this emission mainly originates in the heated glass ampoule. As seen in the insert of Figure 4.3, below $\tilde{\nu} \approx 100$ cm^{-1} the signal is higher than from the Globar. The difference may not seem significant but is indeed important while investigating effects in this low energy range, such as cyclotron resonance in systems with relatively large effective masses of charge carriers.

For measurement in the near infrared to visible light, a tungsten filament heated by electrical current is used as its emission covers the whole visible and part of the infrared range.

4.1.3. Beamspliters

A beamsplitter in the interferometer is another essential part of the spectrometer. An ideal beamsplitter has a 50/50 ratio of transmission and reflection in the whole spectral range, which is rarely achieved in the practical realization over a broader spectral interval. Therefore, different materials have to be used for different spectral ranges where they are close to the ideal ratio.

At low energies of the far infrared range, several millimeters thick silicon can be used [45]. As seen in Figure 4.4, the silicon beamsplitter can be used in a fairly broad range, from few cm^{-1} up to 3000 cm^{-1}, except the range around 600 cm^{-1}, where strong double phonon absorption appears (insert of Figure 4.4).
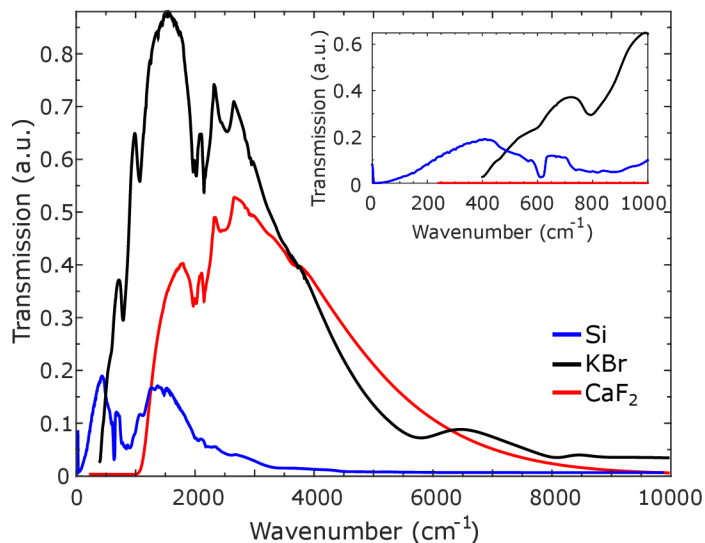

Figure 4.4: Comparison of transmission spectra with different beamsplitters, measured with a Globar$^{\text{TM}}$ source and RT-DLaTGS detector.

Typically, the Si beamsplitter is used only up to 400 cm^{-1} as further, a beamsplitter with a layer of potassium bromide (KBr) shows much better results. The main advantage of the KBr is its broad range of high efficiency. It can be used down to $\tilde{\nu} = 400$ cm^{-1} through the whole middle infrared range and far into the near infrared range. As shown in Figure 4.4 combined with the Globar, in the near infrared range, it even outperforms the recommended calcium fluoride (CaF$_2$) beamsplitter. The main disadvantage of KBr is that it is a hydroscopic material, meaning it absorbs water and deteriorates. Therefore, it is not advised to use KBr beamsplitter for measurements when the atmosphere is present.

4.1.4. Infrared radiation detectors

There are two basic types of detectors of infrared radiation. The quantum detectors measure the quantity of electrons excited to higher states (from the valence to conduction band) via photon absorption. Such a transition will occur only for wavelengths lower than some critical λ_{max}, and photons of higher wavelength are not detected. Because the number of photons increases for a given amount of energy, so does the sensitivity of quantum detectors.

The other type of infrared radiation detectors is thermal detectors, devices operating by sensing the temperature change due to the absorption of radiation. A bolometer is a thermal detector that uses a change of resistance related to its temperature. A material with a high temperature coefficient of resistance (today, for room temperatures, mostly deuterated l-alanine doped triglycine sulfate - DLaTGS) is exposed to the radiation. As the absorbed energy is transformed into heat, the temperature of the bolometer rises, and thus its resistance changes. To minimize the heat exchange between the bolometer and its surroundings, it is suspended in a vacuum on very thin copper wires (Figure 4.5 a)).

To measure the resistance of the bolometer, it is connected in series to a resistor with a similar value of resistance and a constant voltage is applied. As the change in the intensity of incident radiation affects the resistance of the bolometer, the device behaves like a voltage divider (Figure 4.5 b)) and redistributes the applied voltage between the bolometer and the resistor according to their resistance. The measured voltage on the individual parts (either bolometer or resistor), then corresponds to the intensity of incident radiation.
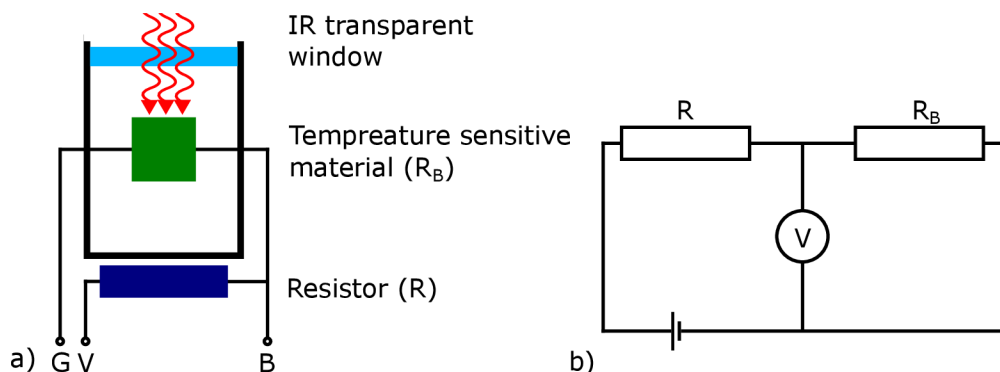
Figure 4.5: a) Simplified bolometer device with indicated wiring and outputs for the voltage (V), ground (G) and voltage on the bolometer (B) b) Equivalent electrical circuit of bolometer device with a constant voltage source and voltmeter to measure the voltage on a bolometer.

Such a device may operate at very low temperatures but it has to be calibrated to the temperature of operation by selecting appropriate resistor as its resistance also change significantly with temperature.

4.2. Ellipsometry

Ellipsometry is a popular optical technique used to precisely determine the dielectric function of a sample by measuring the change in the polarization state of radiation reflected from the sample. The main difference from the conventional reflection measurement is that ellipsometry, besides the amplitude of the reflected light, also captures its phase. Another advantage over reflection measurement is that ellipsometry does not need a reference spectrum for the determination of the measured material's optical properties.

A sample is irradiated by a light characterized by a certain polarization (done by a linear polarizer before the sample) and as the light is reflected from the surface of the sample, the polarization changes. The polarization of reflected light is analyzed and the outcome of measurement are two ellipsometric angles Δ and Ψ defined as:

$$\Delta = \delta_1 - \delta_2, \tag{4.7}$$

where δ_1 is a phase difference between the light component parallel to the plane of incidence (p-component) and a component perpendicular to the plane of incidence (s-component) before the reflection from the sample and δ_2 is after the reflection, and

$$\mathrm{tg}\,\Psi = \left|\frac{r_p}{r_s}\right|, \tag{4.8}$$

where r_p and r_s are amplitudes of p- and s-component of reflected light, respectively.

These two parameters can be combined into one complex quantity ϱ, as:

$$\varrho = \mathrm{tg}\,\Psi e^{i\Delta} = \frac{r_p}{r_s}, \tag{4.9}$$

where $\mathrm{tg}\,\Psi$ takes the role of a magnitude of ϱ and $e^{i\Delta}$ is its phase [34].

When a thickness of the measured sample is known, it is possible to obtain a point by point spectral dependence of the dielectric function. When the measurement is performed at more angles of incidence, it is possible to obtain the dielectric function as well as the thickness of the sample and the roughness of its surface. Ellipsometers that are able to measure at different angles of incidence are called Variable Angle Spectroscopic Ellipsometers (VASE) and the one used for this thesis comprises a rotational compensator (see Figure 4.6) which modifies the light polarization back to linear. Ellipsometers with rotational compensator eliminate the loss of sensitivity for Δ values near 0° or 180°, which occurs in ellipsometers with a rotational analyzer.
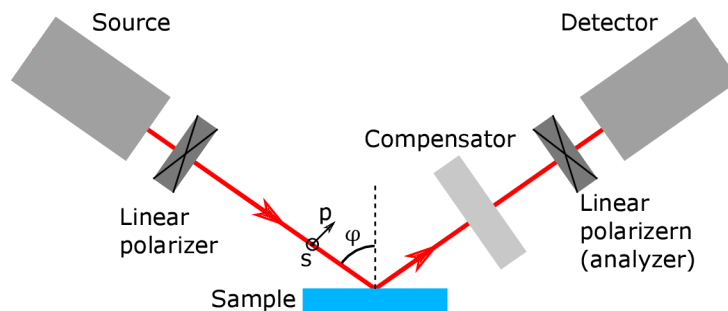

Figure 4.6: Schematic drawing of principal components of ellipsometer with a rotating compensator. The p-component is parallel to the plane of incidence and s-component perpendicular to the plane of incidence.

4.3. Experimental setup for magneto-optical measurement

To measure the optical response in the magnetic field, a spectrometer has to be optically coupled to a magnet. In the infrared range, due to the broad range of the spectrum, which for the purpose of this thesis spans from a few meV up to 1 eV, the use of optical fibers is not possible. Instead, the radiation is guided by metallic tubes, ideally with internal gold coating, which significantly reduces the signal losses and which also avoids the degradation of the waveguide surface.

All magnets used in this thesis have their coil in the vertical position and therefore, the radiation beam has to be reflected from the horizontal spectrometer down to the magnet. A parabolic golden mirror is usually used as it also focuses the beam into the waveguide and onto the sample (Figure 4.7).

A sample on top of the detector is inserted into the probe in which air is replaced by helium gas at low pressure (tens of mbar). The probe is then submerged into the liquid helium in the cryostat so the sample is positioned in the center of the magnet coil.
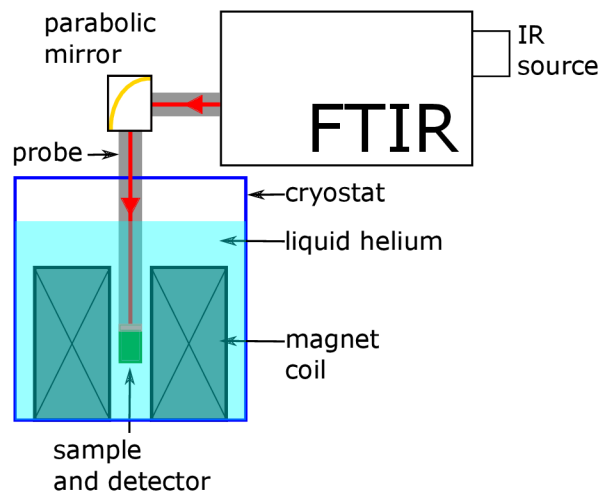

Figure 4.7: Schematics of a magneto-optical setup in a transmission configuration, which consists of a FTIR spectrometer connected via light-pipe optics to the sample on top of a detector inside of a magnet.

As the cryostat is filled with the liquid helium, the magnet coil, the sample and detector are all cooled down to $T = 4.2\,\mathrm{K}$. It is possible to pump down the pressure of helium vapors in the top part of the cryostat to further reduce the temperature down to approximately $T = 1.5\,\mathrm{K}$.

4.3.1. Generation of high magnetic field

The magnetic field is generated by moving charge, or in other words, current running through conducting wire. For a linear wire, the induced magnetic field has a radial shape. More intense and in certain space area also more homogeneous magnetic field can be generated using conducting wire in the shape of a coil. The Ampere's law implies that the magnetic field generated inside such a solenoid is directly proportional to the current I and density of current loops N/l:

$$B(I) = \frac{\mu_0 N}{l} I, \tag{4.10}$$

where μ is the permittivity of vacuum, N is the number of its loops and l is a length of the solenoid.

Superconductive magnets

Superconductive magnets have coils made of materials that become superconducting below a certain critical temperature. These materials undergo a transition to the superconductive state, where they have effectively no resistance and the power consumption for running the magnet at a high magnetic field drops significantly.

There are more ways to achieve temperature low enough to induce such conductor-superconductor transition. One of the simplest is to put the coil inside of the cryostat with liquid helium that keeps its temperature at $T = 4.2\,\mathrm{K}$. Additionally, the cryostat may have a liquid nitrogen shielding ($T \approx 77\,\mathrm{K}$), that will slow down the evaporation of more expensive helium.

The superconductive coil is usually powered by a low voltage DC power supply that can generate high current, resulting in very low power consumption. Another advantage of superconducting magnets is the possibility of a persistent mode. A superconducting switch, connecting both terminals of the coil, can be switch on and off by decreasing or increasing its temperature, respectively. When the superconducting switch is turned on, the magnet enters a persistent mode, the coil becomes a superconducting loop and there is no energy dissipated. At this point, the current running through the coil stays constant, resulting in a stable magnetic field, with no power consumption. Additionally, the magnetic field's stability in the persistent mode is better than with most power supplies.

The maximum magnetic field generated by the superconducting magnet is limited by the current running through the coil and its temperature. When the current exceeds a certain threshold, the superconducting coil does undergo a transition back to the non-superconducting state, rapidly heats up and possibly does damage the magnet.

Resistive magnets

Unlike the superconductive magnets, resistive magnets are made from metals and its alloys that exhibit very low, but still non-zero resistance. The alloys used to construct high-field resistive coils are mostly composed of copper and silver.

The resistive magnets are not limited by the superconductivity condition and, therefore, at the cost of high power consumption, can generate a much stronger magnetic field (in principle, independent on the temperature of the magnet). Its maximum field is limited mostly by an electric power supply, but also by its mechanical strength as the magnet tend to expand due to the magnetic field. Because of the non-zero resistance, the supplied power is transformed to Joule heat and that has to be dissipated away from the coil. The heat dissipation is done by water flowing through the magnet, simultaneously bringing vibrations to the whole system that decrease the signal-to-noise ratio. As the resistive magnets are generally more complicated and there is lower demand for resistive magnets over superconducting coils, they are also more expensive.

At the LNCMI Grenoble, there are seven resistive magnets supported by a $24\,\mathrm{MW}$ power supply, that can generate a magnetic field up to $37\,\mathrm{T}$. While operational, these magnets are cooled by a closed-loop of water with a typical flow rate of nearly $1\,000\,\mathrm{m^3 h^{-1}}$.

4. INFRARED SPECTROSCOPY

5. Experimental results

The main goal of the experimental part of this thesis is the characterization of $Bi_2\,Te_3$ sample using various methods such as magneto-spectroscopy, ellipsometry and magneto-transport. Additionally, thin layers of ScPtBi, material predicted to exhibit topological properties, were characterized by magneto-transport measurements.

5.1. Magneto-optical spectroscopy of $Bi_2\,Te_3$

The magneto-optical experiments were conducted in cooperation with the National laboratory of high magnetic fields (LNCMI) in Grenoble, France. The studied epilayer of Bi_2Te_3 was grown using molecular beam epitaxy on a (111) face of a 1 mm thick BaF_2. To determine its transport properties, a magneto-transport measurement in the Van der Pauw configuration was performed to confirm holes as major charge carriers and their density as $n_h \approx 2 \times 10^{18}$ cm^{-3}. The magneto-optical data were acquired by a commercial FTIR spectrometer Bruker Vertex 80v, coupled to superconducting solenoid (B up to 13 T) or resistive magnet ($B = 13 - 34$ T) via light-pipe optics. The sample was measured at $T = 2\,K$ in a Faraday configuration ($\boldsymbol{B} \parallel \boldsymbol{k}$) and with a magnetic field parallel to the c-axes (see Figure 2.5). The measured transmission spectra T_B, are normalised by zero-field transmission T_0, and relative magneto-absorbance was calculated as: $A_B = -\ln[T_B/T_0]$.

The magneto-optical data collected on the studied Bi_2Te_3 epilayer in the middle infrared spectral range are presented in Figures 5.1 a) and b), as a stacked-plot and false-color plot of relative magneto-absorbance spectra, respectively. The baseline tilt and offset of individual relative magneto-absorbance spectra are corrected to be flat and zero by subtracting linear function from individual spectra. The red line in Figures 5.1 b) and 5.2 indicates a transit between the superconducting coil and resistive magnet. The magneto-optical data shows a rather complex response comprising a series of pronounced resonances with a non-linear B dependence. In the limit of the vanishing magnetic field, the resonances extrapolate to a finite (positive) energy. These resonances are interpreted as inter-Landau level excitations that promote electrons across the band gap. The resonances have pronounced high-energy tails that are typical of interband inter-Landau level excitations in bulk systems.

A more detailed analysis shows the presence of additional transitions with a considerably weaker intensity. These latter transitions become clearly visible in the second derivative of relative magneto-absorbance, plotted as a false-color plot in Figure 5.2 a). Since the observed resonances are relatively sharp, we associate the minima in $d^2 A_B/d\omega^2$ curves directly with the positions of excitations. No resonances attributable to surface states were identified, in contrast to preceding studies [46].

Let us now compare our experimental data with expectations based on the two-band model proposed in Section 3.3. In the first step, we assign the series of dominant tran-
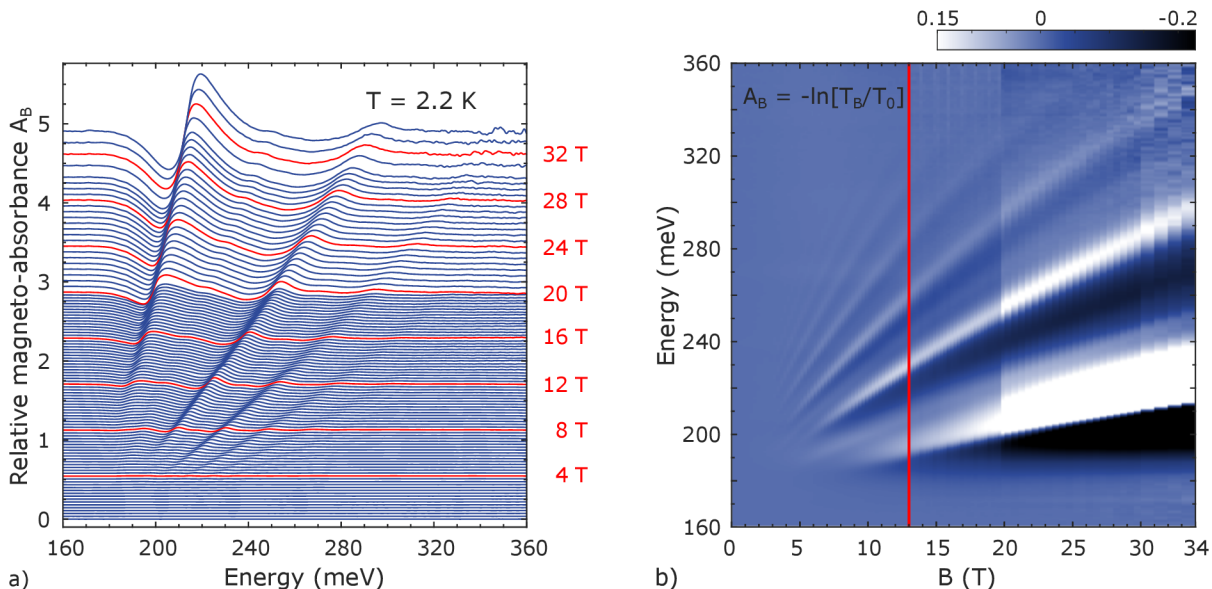
Figure 5.1: a): Baseline-corrected relative magneto-absorbance spectra, $A_B = -\ln[T_B/T_0]$, plotted for selected values of the applied magnetic field. The maxima correspond to individual inter-Landau level resonances. The subsequent spectra were shifted vertically by the offset scaling linearly with B. b): The false-color plot of relative magneto-absorbance, A_B.

sitions, which contain up to eight well-resolved lines, with the position of $n \to n \pm 1$ resonances expected in a system with the full rotational symmetry. Almost perfect agreement is found for an energy band gap $E_g = 2\Delta = (175 \pm 5)$ meV and a velocity parameter $v_D = (4.7 \pm 0.1) \times 10^5 \text{ms}^{-1}$, as shown by blue lines in Figure 5.2 b). In this way, all dominant lines may be explained using only one widely tunable parameter v_D. That is because the band gap 2Δ falls into a fairly narrow interval given by the zero-field extrapolation of lines.

The parameters Δ and v_D deduced from the fit of dominant interband transitions allows us to predict the position and B-dependence of the fundamental cyclotron resonance (CR) mode, $1 \to 0$, in our p-type sample (cf. Figure 3.4). The expected position matches very well the experimental data (red solid line in Figure 5.3 a)) without any additional adjustment of v_D or Δ. The cyclotron energy deviates only weakly from a linear dependence in B. That allows us to describe it approximately by the formula for the cyclotron energy of a parabolically dispersing particle: $\hbar\omega_c = \hbar eB/m_D$ using the Dirac mass of $m_D = 0.07m_0$ (dashed gray line in Figure 5.3). This value is in very good agreement with preceding magneto-transport studies, which for holes reported the band-edge mass of $0.08m_0$ [33].

Importantly, our model does not include any electron-hole asymmetry. The experimentally deduced Dirac mass m_D thus represents a good estimate of the band-edge mass for both, holes and electrons. Indeed, the extracted Dirac mass of $m_D = 0.07m_0$ is close to the electron band-edge mass of $0.06m_0$ deduced in the past in quantum oscillation experiments [32]. Importantly, this latter agreement indicates that the conduction-band minimum, hosting the final states of the observed interband inter-Landau level excitations,
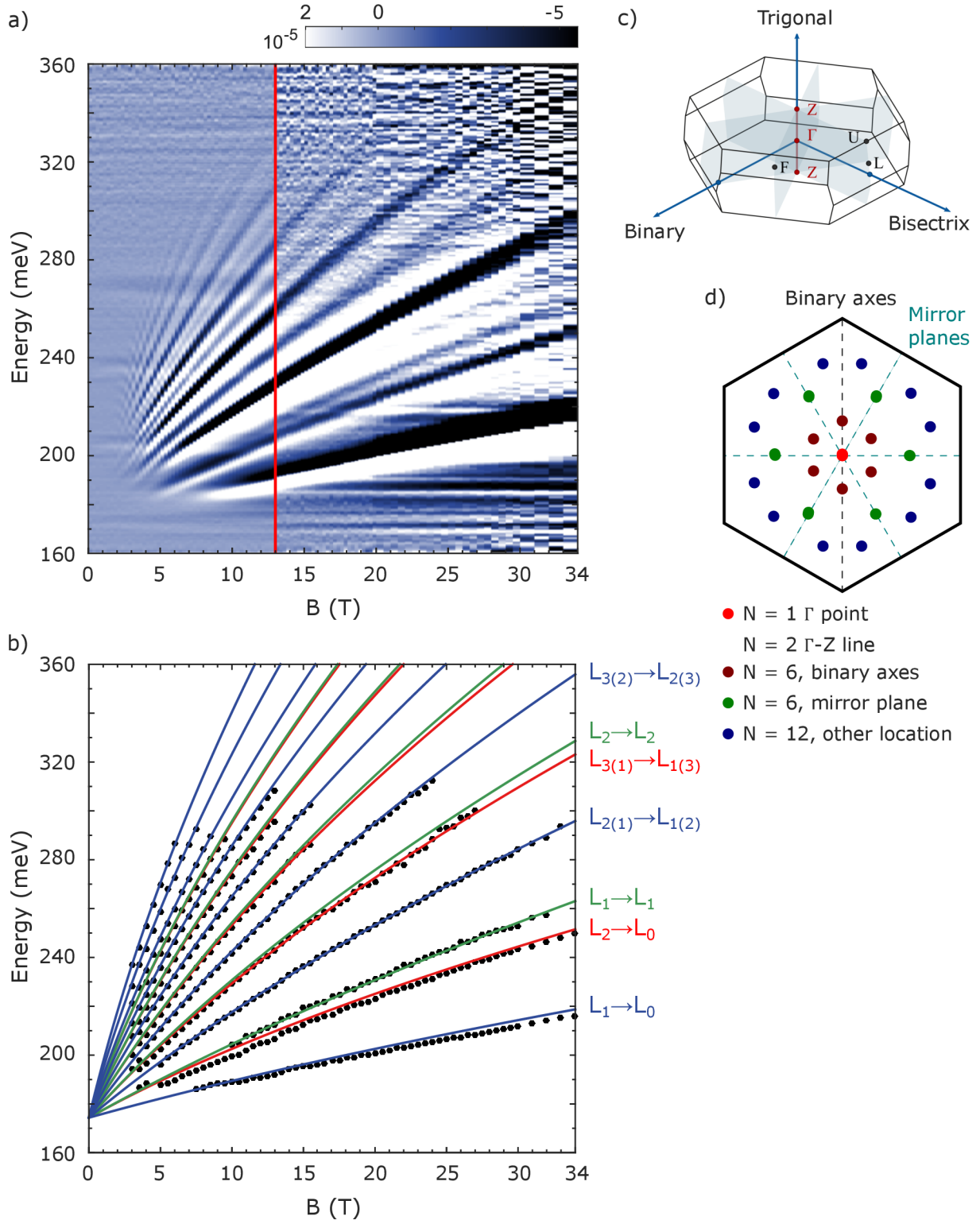
Figure 5.2: a) The false-color plot of the second derivative of relative magneto-absorbance in the middle infrared spectral range, $\mathrm{d}^2/\mathrm{d}\omega^2(-\ln[T_\mathrm{B}/T_0])$. b) Plot of local minima of the $\mathrm{d}^2/\mathrm{d}\omega^2 A_\mathrm{B}$ and theoretically expected positions of interband inter-Landau level transitions that follow three different selection rules: $n \to n\pm1$ (blue), $n \to n$ (green) and $n \to n\pm2$ (red). c) Schematic view of first Brillouin zone d) Possible positions of band gap in the Brillouin zone and their corresponding multiplicity.

is not just a local extremum but the global one. The parameter 2Δ thus corresponds to the fundamental band gap in Bi_2Te_3. Hypothetically, one can imagine that other extrema of the conduction and valence bands exist, which are characterized by the band-edge masses identical to valleys probed in our magneto-optical experiments. In such a case, the real energy band gap might still be smaller and indirect. However, we do not find such a coincidence probable.

Excellent agreement between experimental data and our simple two-band model suggests that Bi_2Te_3 is a direct-gap semiconductor. However, one can never exclude a small displacement δk_{c-v} between the extrema of the conduction and valence bands. Thanks to our low-field magneto-optical data, we may find the upper limit of such a displacement. Approximately, it is given by the reciprocal value of the magnetic length, taken at the onset of Landau level quantization in our sample, $B \approx 3$ T, $\delta k_{c-v} \sim 1/l_B = \sqrt{eB/\hbar} \approx 0.07$ nm^{-1}. Such a distance represents only a small fraction of the whole Brillouin zone size. That allows us to speak about the direct character of the band gap in Bi_2Te_3 with reasonable justification.
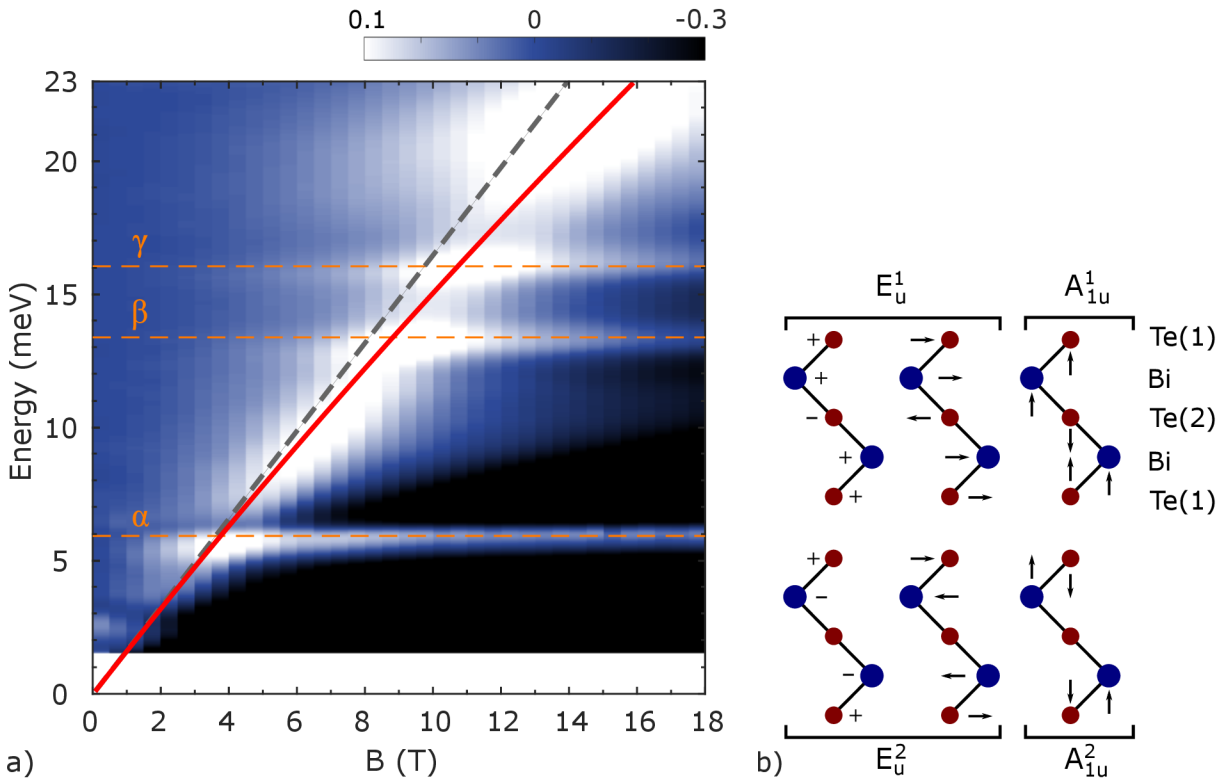

Figure 5.3: The false-color plot of relative magneto-absorbance A_B in the far infrared range with the single CR mode that disperses nearly linear with B. The solid red line corresponds to the energy of the fundamental CR mode, $1 \to 0$, calculated within the two-band model (cf. Figure 3.4). The dashed gray line shows the cyclotron energy, $\hbar\omega_c = \hbar eB/m_D$, for the band-edge (Dirac) mass $m = \Delta/v_D^2 = 0.07m_0$. The horizontal dashed lines show positions of three phonon modes (α, β and γ) to which the CR mode couples. One may associate them with E_u^1, E_u^2 and A_{1u} infrared-active phonons [47]. The last mode is supposed to be active for the electric-field component along the c axis, and it appears since the radiation is focused on the sample using a cone.

In the second step, we compare the positions of additional lines – with weaker integral intensities but still clearly manifested in spectra – with the energies of other possibly

existing inter-Landau level excitations. As a matter of fact, all additionally observed lines fit perfectly to two series: $n \to n \pm 2$ and $n \to n$ marked by red and green lines in Figure 5.2, respectively. These two series nearly overlap for higher indices n, nevertheless, at low photon energies, one may clearly distinguish two separate $2 \to 0$ and $1 \to 1$ lines. Let us notice that the $0 \to 2$ transition should not appear due to the occupation effect in our p-type sample. The proposed two-band model, implying not more than two tunable parameters, is thus capable of explaining all intraband and interband inter-Landau level excitations resolved in our magneto-optical data (more than ten lines). That strongly corroborates our interpretation.

A discussed in Section 3.4, the additionally appearing inter-Landau level excitations reflect the symmetry of electronic bands at the fundamental band gap. The presence of the $n \to n$ series indicates that the symmetry is definitely lower than the trigonal one. Therefore, the direct fundamental gap, evidenced in our magneto-optical experiment, cannot be located on the trigonal axis of Bi_2Te_3. Unless some accidental degeneracy occurs, the valley degeneracy must reach either $N = 6$ for a position in the mirror plane or binary axes or $N = 12$ for any other arbitrary point in the Brillouin zone (see Figure 5.2 c) and, d)). Both possibilities have been discussed in the literature. The former one has been concluded as more probable based on quantum oscillations experiments [32, 33, 48–50].

5.2. Ellipsometry

The previously presented magneto-optical data are complemented by low-temperature ellipsometric measurement in the middle infrared range. By modeling the optical response, it was possible to determine the thickness of the layer as 300 nm and its surface roughness. With these parameters we also obtained the point by point, dielectric function $\varepsilon = \varepsilon_1 + i\varepsilon_2$ shown in Figure 5.4 a). Corresponding real part of optical conductivity, displayed in Figure 5.4 b), was calculated as $\sigma_1 = \varepsilon_0 \omega \varepsilon_2$.

Let us confront our conclusions – about the size, nature and multiplicity of the fundamental band gap in Bi_2Te_3 – with the zero-field optical response obtained using ellipsometry. In line with expectations, the deduced optical conductivity (Figure 5.4 b)) shows a rather steep increase at photon energies slightly above the band gap $E_g = 175$ meV estimated from our magneto-optical experiments.

Similar to conventional semiconductors, the position of the absorption onset shifts to lower energies with increasing T (inset of Figure 5.4). In this way, we may estimate that, at higher temperatures, the energy band gap shrinks roughly linearly with T: $E_g(\text{meV}) \approx 175 - 0.07 \times T[\text{K}]$. Interestingly, the optical conductivity remains non-zero, nearly temperature-independent and flat at photon energies below E_g. Sometimes this behavior is interpreted as the optical response of the surface states, which we assign to excitations from/to localized states in the band gap.

Above the optical band gap, $\sigma_1(\omega)$ in Bi_2Te_3 reaches significantly larger values as compared to the sister compound Bi_2Se_3 (see Figure 5.4 b) and Ref. [51]). The latter has a similar (inverted) direct band gap located at the Γ point [14] and the electronic bands are also fairly well described by the Dirac Hamiltonian for massive electrons [36]. The difference in $\sigma_1(\omega)$ thus must lie in specific band structure parameters, in the reduced mass defined as $\mu = m_e m_h / (m_e + m_h)$ and/or valley degeneracy N, in particular. Assuming strictly parabolic profiles of bands, optical conductivity of direct-gap semiconductor can be approximated as: $\sigma_1(\omega) \propto N \mu^{3/2} \sqrt{\hbar \omega - E_g}$ [2]. Comparing the reduced masses only,
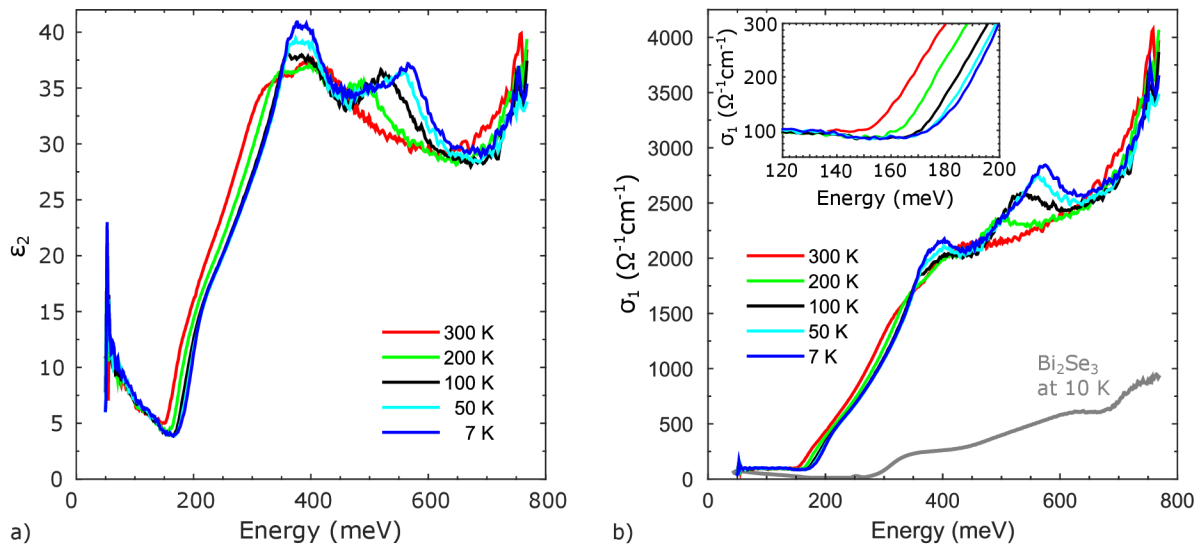
5. EXPERIMENTAL RESULTS

Figure 5.4: The real part of optical conductivity, $\sigma_1(\omega)$, of the studied Bi_2Te_3 sample at the selected temperatures measured using the ellipsometry technique. For comparison, the optical conductivity spectrum of Bi_2Se_3 has been reprinted from [51], see the main text. Due to the Moss-Burstein effect [14, 52], the onset of interband absorption is around 300 meV in this particular Bi_2Se_3 sample, which is well above the energy band gap of 200 meV. The inset shows the sharp increase of $\sigma_1(\omega)$ due to the onset of interband excitations in Bi_2Te_3 in detail.

$\mu_{Bi_2Se_3} = 0.08m_0$ [36] and $\mu_{Bi_2Te_3} = 0.035m_0$, one expects greater σ_1 for Bi_2Se_3, roughly by a factor of 3. In experimental data, however, opposite behaviour is observed (Figure 5.4 b)). Above the corresponding optical band gaps, $\sigma_1(\omega)$ for Bi_2Se_3 is roughly by a factor of 5 smaller as compared to Bi_2Te_3. The valley multiplicity $N = 12$ thus appears to be more consistent with our optical data on Bi_2Te_3 as compared to $N = 6$, concluded in the above-cited transport studies. Nevertheless, this rule of thumb analysis provides us with only a very rough guide, especially when a very strong anisotropy along the c-axis ($\mu^{3/2} \rightarrow \mu_\parallel \mu_c^{1/2}$) was completely neglected. The anisotropy in Bi_2Te_3 may considerably differ from that in Bi_2Se_3 and it cannot be deduced from the presented magneto-optical data, which provide us only with the in-plane (i.e., perpendicular to the trigonal axis) estimate of the velocity parameter.

The applicability of the simple massive Dirac model to the magneto-optical response of Bi_2Te_3 may be somewhat surprising. In fact, the generic two-band models for 2D or 3D topological insulators [4, 6, 15, 35] always comprise dispersive diagonal elements, $\Delta \rightarrow \Delta + Mk^2$ which account for the band inversion. These dispersive diagonal elements are responsible for the appearance of the surface states, but they also profoundly affect bulk properties. For instance, when the magnetic field is applied, they lead to characteristic (anti)crossing of zero-mode ($n = 0$) Landau levels in all inverted systems [6, 36, 53–55].

Even though Bi_2Te_3 is a topological insulator – with inverted bands and experimentally confirmed surface states [16, 25, 56] – such diagonal dispersive terms are not included in our model (3.18), which thus keeps the simplest possible massive-Dirac form. That is, for instance, seen from the deduced electron and hole masses that approach very well the Dirac mass m_D. That contrasts with Bi_2Se_3, where the massive Dirac picture is also valid [36], nevertheless, the presence of the dispersive diagonal elements in the Hamiltonian enhances twice the mass of electrons and holes as compared to the Dirac mass.

To explain the absence of the dispersive terms on the diagonal of the Hamiltonian (3.18), let us note that the region with the inverted ordering of bands represents only a small part of the Brillouin zone of Bi_2Te_3. It is located around the Γ point [57] and it does not coincide with the location of the fundamental band gap. That also implies that the velocity parameter v_D deduced from our experiments on Bi_2Te_3 is not connected with the slope of the linear bands on the surface, which emerge due to the band inversion at the Γ point. Again, this is in contrast to other topological insulators such as Bi_2Se_3 or $Bi_{1-x}Sb_x$ where the regions of the fundamental band gap and of the band inversion overlap, and where, the slope of the conical surface band provide us with a reasonable estimate for the velocity parameter in the Hamiltonian describing bulk states.

5.3. Magneto-transport measurements of ScPtBi

The second part of the experiment section of this thesis is dedicated to a magneto-transport characterization of polycrystalline ScPtBi layers, another interesting member of the topological insulator family [58]. The samples were prepared by Özgür Polat, Ph.D., at the CEITEC Nano. These layers are approximately 60 nm thick and were grown by magnetron sputtering on silicon oxide (SiO_2) or aluminium oxide (Al_2O_3) substrate. Theoretical calculations for ScPtBi indicate the electronic band structure similar to HgTe [58, 59]. Therefore it should be possible to observe topologically protected states in strained ScPtBi or ScPtBi based quantum wells, surrounded by ScPtSb. A study done on a monocrystalline ScPtBi [60], presents a large value of magneto-resistance of 240 % at $T = 2$ K for magnetic field $B = 1$ T. However, the monocrystals were not found to exhibit topological properties and the large magneto-resistance was explained by the weak antilocalization (WAL) effect in bulk and magnetic field induced metal-semimetal transition [60].

The longitudinal magneto-resistance of the studied layers prepared under various growth conditions (parameters in Table 5.3), was measured, with the applied current $\boldsymbol{I}$ perpendicular to the out-of plane magnetic field $\boldsymbol{B}$ (see Figure 5.5 d)). The magneto-transport measurements were performed at varying temperatures from $T = 300$ K down to 5 K in magnetic field up to $B = 9$ T. The magneto-resistance data of measured sample for current $I = 10$ µA, calculated as $MR(B) = [R(B) - R(0)]/R(0) \cdot 100\%$, are presented in Figure 5.5 a), b) and c). Our data show rather small values of magneto-resistance $\approx 24\%$ at 9 T, which is much lower as compared to large magneto-resistance measured in monocrystals [60]. Since the correct stoichiometry was verified by XPS spectroscopy, such a significant difference in magneto-resistance is most probably caused by the polycrystalline nature of our samples.

Table 5.1: Growth parameters of studied ScPtBi layers.

Sample	Substrate	Temperature	Capping layer	...
51-B	Al_2O_3 (1121)	300 °C	-	
57-A	Si (111)	300 °C	Al	
58-A	Si (111)	200 °C	Al	

To determine the transport properties, low-field magneto-conductance in a form of $\Delta G(B) = G(B) - G(0)$ was calculated and plotted in Figure 5.6. The magneto-conductance $\Delta G(B)$ was fitted using the Hikami-Larkin-Nagaoka (HLN) formula:
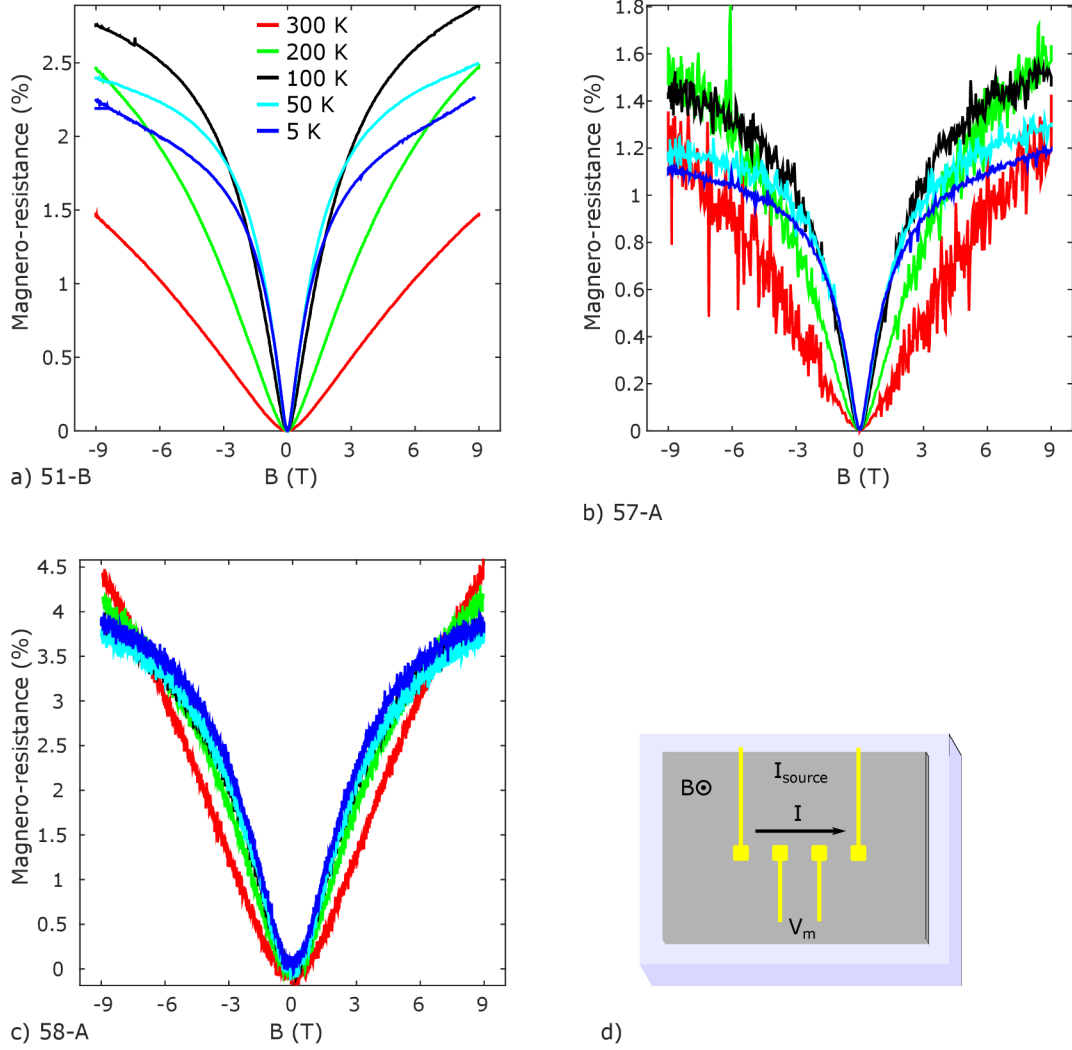
Figure 5.5: a) b) and c) Measurement of magneto-resistance at different temperatures of ScPtBi samples 51-B, 57-A and 58-A respectively. d) The schematic drawing of magneto-resistance measurement with electrical current $\boldsymbol{I}$ perpendicular to the (out-of plane) magnetic field $\boldsymbol{B}$.

$$\Delta G(B) = \frac{\alpha e^2}{2\pi^2\hbar}\left[\psi\left(\frac{1}{2} + \frac{\hbar}{4eBl_\varphi^2}\right) - \ln\left(\frac{\hbar}{4eBl_\varphi^2}\right)\right], \qquad (5.1)$$

where ψ is the digamma function, l_φ is the phase coherence length, and α it the prefactor, indicating a strength of spin-orbit interaction and magnetic scattering [61]. The fit parameters α and l_φ for various temperatures are listed in Table 5.3.

The prefactor α value for an ideal single 2D conducting channel is -0.5, which also corresponds to no magnetic scattering and strong spin-orbital interaction. For a multi-channel conduction (surface and bulk) the prefactor α lies between -0.5 and -1.5 [61, 62]. In our experimental data, the value of α is higher than expected for a 2D topological insulator, however, it is six orders of magnitude lower then values reported in a study of monocrystalline ScPtBi.
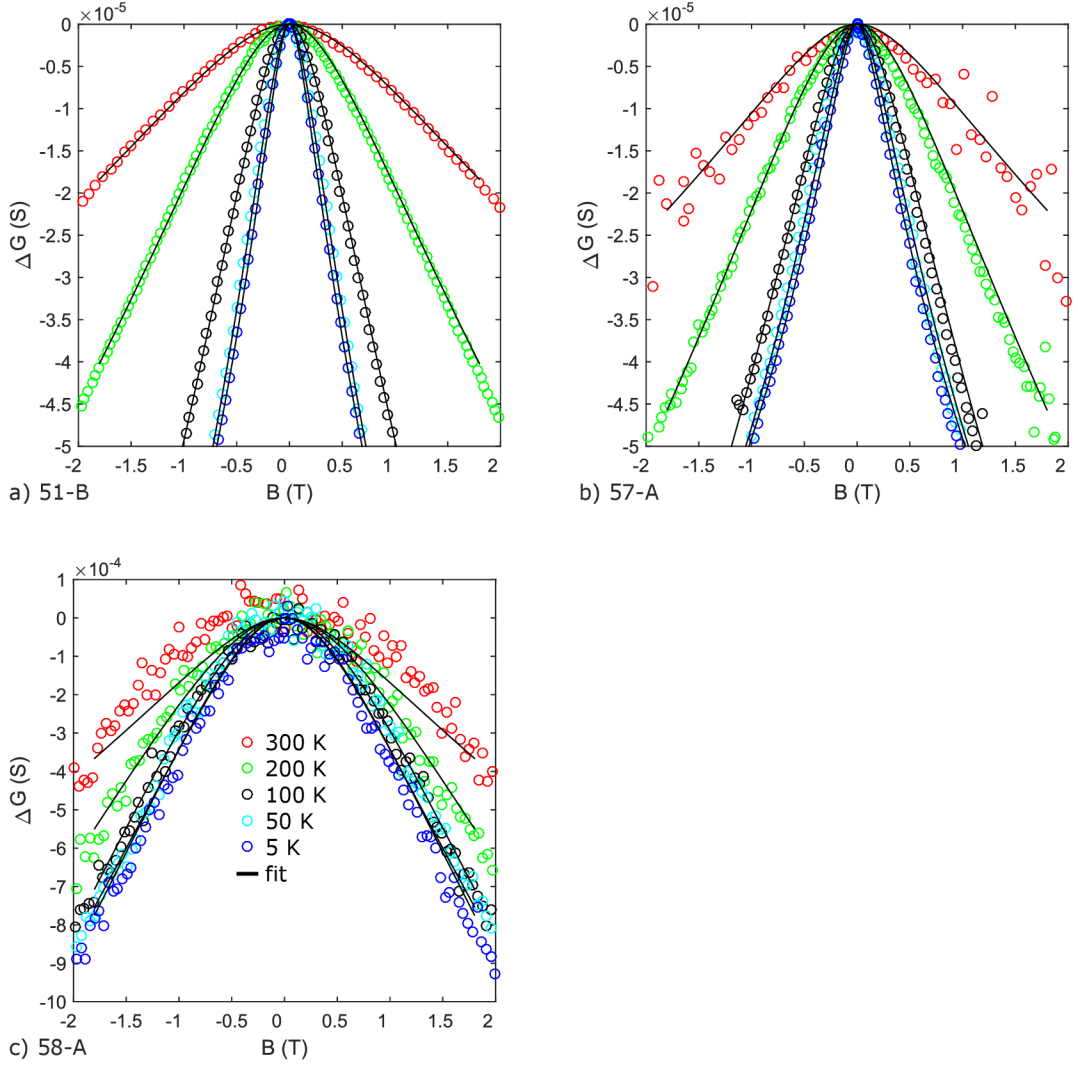
Figure 5.6: The magneto-conductivity corresponding to $\Delta G(B) = G(B) - G(0)$ is plotted (circle markers), and fitted using the HLN formula (5.1) (black lines). Corresponding fit parameters α and l_φ for different temperatures are presented in Table 5.3

Table 5.2: Values of fit parameters α and l_φ for measured samples at varying temperatures.

Sample	Parameter	300 K	200 K	50 K	5 K
51-B	α	-5.52 ± 0.08	-8.4 ± 0.1	-7.40 ± 0.08	-5.9 ± 0.1
	$l_\varphi \ (nm)$	18.28 ± 0.08	21.3 ± 0.1	39.6 ± 0.3	46.0 ± 0.6
57-A	α	-4.7 ± 0.9	-9.3 ± 0.3	-5.8 ± 0.2	-4.57 ± 0.09
	$l_\varphi \ (nm)$	21 ± 1	21.5 ± 0.2	37.6 ± 0.9	-44.0 ± 0.6
58-A	α	-220 ± 20	-90 ± 8	-280 ± 10	-196 ± 7
	$l_\varphi \ (nm)$	13.8 ± 0.3	19.8 ± 0.6	16.4 ± 0.1	19.4 ± 0.2

5. EXPERIMENTAL RESULTS

6. Conclusion

The goal of this thesis was the characterization of the topological insulator Bi_2Te_3, mainly clarifying the properties of its band gap. The first part of the thesis is dedicated to reviewing of research done on topological insulators with a focus on the Bi-Se-Te family and especially, Bi_2Te_3. The optical response of solid matter in a magnetic field is discussed as well as the experimental setup for Landau level spectroscopy.

In the experimental part of the thesis, a thin layer of epitaxial Bi_2Te_3, grown at the JKU Linz, was studied via Landau level spectroscopy in a magnetic field up to $34\,T$ at the LNCMI in Grenoble. In a middle infrared range ($E = 150 - 400$ meV), a series of resonances were observed. They were interpreted as inter-Landau level excitations that promote electrons across the band gap. In a limit of the vanishing magnetic field, these resonances extrapolate to the energy of $E = 175 \pm 5$ meV, which corresponds to the energy of the band gap E_g. These resonances were compared to a two-band model of Dirac massive fermions with direct band gap and almost perfect agreement of experimental data and proposed model was found, for parameters $E_g = 175 \pm 5$ meV and $v_D = 4.5 \pm 0.1 \times 10^5$ ms^{-1}. By further analysis of the selection rules of excitations present in measured spectra, it was concluded that the symmetry of the band gap is lower than trigonal, and therefore, it is positioned outside of trigonal axes. This argument is also supported by the absence of band inversion parameter in our model that is already experimentally confirmed to be present near the Γ point of the Brillouin zone. The fundamental band gap then displays either sixfold valley degeneracy, for a position in the mirror planes or on the binary axis, or twelvefold valley degeneracy for an arbitrary point in the Brillouin zone.

The magneto-optical study was supplemented by an ellipsometric measurement done at the CEITEC Nano in Brno. By comparison with previously studied Bi_2Se_3 [51], it was found that the real part of optical conductivity σ_1 of Bi_2Te_3 is almost 5 times higher than of Bi_2Se_3 in the region above the band gap. As the approximate examination of effective masses in both materials show that the σ_1 of Bi_2Se_3 should be three times larger, the twelvefold valley degeneracy of Bi_2Te_3 seems to be more consistent. However, further investigation will have to be carried out to determine the band gap position more precisely.

Additionally to the Bi_2Te_3, magneto-transport of ScPtBi was performed. Low field magneto-conductance was fitted using the Hikami-Larkin-Nagaoka formula, and fitting parameters for various temperatures are presented. The results suggest that the studied samples do not exhibit topological properties, and also indicate stronger spin-orbital interaction and lower magnetic scattering for polycrystalline ScPtBi layers then monocrystalline ScPtBi crystals.

6. CONCLUSION

References

[1] MOHELSKY, I., A. DUBROKA, J. WYZULA, A. SLOBODENIUK, G. MARTINEZ, Y. KRUPKO, B. A. PIOT, O. CAHA, J. HUMLICEK, G. BAUER, G. SPRINGHOLZ and M. ORLITA. Landau level spectroscopy of Bi_2Te_3. *arXiv:2004.13565*. 2020.

[2] YU, P. Y. and M. CARDONA. *Fundamentals of semiconductors: physics and materials properties*. Springer, 1996.

[3] HASAN, M. Z. and C. L. KANE. *Colloquium:* Topological Insulators. *Reviews of Modern Physics*. 2010, vol. 82, 3045.

[4] BERNEVIG, B. A., T. L. HUGHES and S.-C. ZHANG. Quantum Spin Hall Effect and Topological Phase Transition in HgTe Quantum Wells. *Science*. 2006, vol. 314, 1757–1761.

[5] PANKRATOV, O. A., S. V. PAKHOMOV and B. A. VOLKOV. Supersymmetry in heterojunctions: Band-inverting contact on the basis of $Pb_{1-x}Sn_xTe$ and $Hg_{1-x}Cd_xTe$. *Solid State Communications*. 1987, vol. 61, 93–96.

[6] KÖNIG, M., S. WIEDMANN, C. BRÜNE, A. ROTH, H. BUHMANN, Molenkamp L. W. and at AL. Quantum Spin Hall Insulator State in HgTe Quantum Wells. *Science*. 2007, vol. 318, 766–770.

[7] LIANG, F. and C. L. KANE. Topological Insulators with Inversion Symmetry. *Physical Review B*. 2007, vol. 76, 045302.

[8] MOORE, J. E. and L. BALENTS. Topological invariants of time-reversal-invariant band structures. *Physical Review B*. 2007, vol. 75, 121306(R).

[9] ROY, R. Three dimensional topological invariants for time reversal invariant Hamiltonians and the three dimensional quantum spin Hall effect. *Physical Review B*. 2009, vol. 79, 195322.

[10] HSIEH, D., D. QIAN, L. WRAY, Y. XIA, Y. S. HOR, R. J. CAVA and M. Z. HASAN. A topological Dirac insulator in a quantum spin Hall phase. *Nature*. 2008, vol. 452, 9970–974.

[11] WOLFF, P. A. Matrix elements and selection rules for the two-band model of bismuth. *Journal of Physics and Chemistry of Solids*. 1964, vol. 25, 1057–1068.

[12] MOORE, J. E. The next generation. *Nature Physics*. 2009, vol. 5, 378–380.

[13] XIA, Y., D. QIAN, D. HSIEH, L. WRAY, A. PAL, H. LIN, A. BANSIL, D. GRAUER, Y. S. HOR, R. J. CAVA and M. Z. HASAN. Observation of a large-gap topological-insulator class with a single Dirac cone on the surface. *Nature Physics*. 2009, vol. 5, 398–402.

REFERENCES

[14] MARTINEZ, G., B. A. PIOT, M. HAKL, M. POTEMSKI, Y. S. HOR, A. MATERNA, S. G. STRZELECKA, A. HRUBAN, O. CAHA, J. NOVÁK, A. DUBROKA, Č. DRAŠAR and M. ORLITA. Determination of the energy band gap of Bi_2Se_2. *Scientific Reports*. 2017, vol. 7, 6891.

[15] ZHANG, H., C.-X. LIU, X-L. QI, X. DAI, Z. FANG and S.-C. ZHANG. Topological insulators in Bi_2Se_3, Bi_2Te_3 and Sb_2Te_3 with a single Dirac cone on the surface. *Nature Physics*. 2009, vol. 5, 438–442.

[16] HSIEH, D., Y. XIA, D. QIAN, L. WRAY, F. MEIER, J. H. DIL, J. OSTERWALDER, L. PATTHEY, A. V. FEDOROV, H. LIN, A. BANSIL, D. GRAUER, Y.S. HOR, R. J. CAVA and M. Z. HASAN. Observation of Time-Reversal-Protected Single-Dirac-Cone Topological-Insulator States in Bi_2Te_3 and Sb_2Te_3. *Physical Review Letters*. 2009, vol. 103, 146401.

[17] NOH, H.-J., H. KOH, S. J. OH, J. H. PARK, H. D. KIM, J. D. RAMEAU, T. VALLA, T. KIDD, P. D. JOHNSON, Y. HU and Q. LI. Spin-orbit interaction effect in the electronic structure of Bi_2Te_3 observed by angle-resolved photoemission spectroscopy. *EPL*. 2008, vol. 81, 57006.

[18] WRIGHT, D. A. Thermoelectric properties of Bismuth Telluride and its alloys. *Nature*. 1958, vol. 181, no. 4612, 834–834. Available from: doi:10.1038/181834a0.

[19] WITTING, I. T., T. C. CHASAPIS, F. RICCI, M. PETERS, N. A. HEINZ, G. HAUTIER and S. G. JEFFREY. The Thermoelectric Properties of Bismuth Telluride. *Advanced Electronic Materials*. 2019, vol. 5, no. 6, 1800904. Available from: doi:10.1002/aelm.201800904.

[20] CAHA, O., A. DUBROKA, J. HUMLICEK, V. HOLY, H. STEINER, M. UL-HASSAN, J. SANCHEZ-BARRIGA, O. RADER, T. N. STANISLAVCHUK, A. A. SIRENKO, G. BAUER and G. SPRINGHOLZ. Growth, Structure, and Electronic Properties of Epitaxial Bismuth Telluride Topological Insulator Films on BaF_2 (111) Substrates. *Crystal growth and design*. 2013, vol. 13, 3365–3373.

[21] GOLDSMID, H. J. Bismuth Telluride and Its Alloys as Materials for Thermoelectric Generation. *Materials*. 2014, vol. 7, 2577–2592.

[22] KAISER, W., W. G. SPITZER, R. H. KAISER and L. E. HOWARTH. Infrared Properties of CaF_2, SrF_2, and BaF_2. *Physical Review*. 1962, vol. 127, 1950–1954.

[23] POHL, Udo W. *Epitaxy of Semiconductors: Introduction to Physical Principles*. Springer, 2013.

[24] STEINER, Hubert, Valentine VOLOBUEV, Ondřej CAHA, Günther BAUER, Gunther SPRINGHOLZ and Václav HOLÝ. Structure and composition of bismuth telluride topological insulators grown by molecular beam epitaxy. *Journal of Applied Crystallography*. 2014, vol. 47, no. 6, 1889–1900.

[25] CHEN, Y. L., J. G. ANALYTIS, J.-H. CHU, Z. K. LIU, S.-K. MO, X. L. QI, H. J. ZHANG, D. H. LU, X. DAI, Z. FANG, S. C. ZHANG, I. R. FISHER, Z. HUSSAIN and Z.-X. SHEN. Experimental Realization of a Three-Dimensional Topological Insulator, Bi_2Te_3. *Science*. 2009, vol. 325, 178–181.

[26] ALPICHSHEV, Z., J. G. ANALYTIS, J.-H. CHU, I. R. FISHER, Y. L. CHEN, Z. X. SHEN, A. FANG and A. KAPITULNIK. STM Imaging of Electronic Waves on the Surface of Bi_2Te_3: Topologically Protected Surface States and Hexagonal Warping Effects. *Physical Review Letters*. 2010, vol. 104, 016401.

[27] MISHRA, S. K., S. SATPATHY and O. JEPSEN. Electronic structure and thermoelectric properties of bismuth telluride and bismuth selenide. *Journal of Physics: Condensed Matter*. 1997, vol. 9.

[28] YOUN, S. J. and A. J. FREEMAN. First-principles electronic structure and its relation to thermoelectric properties of Bi_2Te_3. *Physical Review B*. 2001, vol. 63, 085112.

[29] NECHAEV, I. A. and E. V. CHULKOV. Quasiparticle band gap in the topological insulator Bi_2Te_3. *Physical Review B*. 2013, vol. 88, 165135.

[30] MICHIARDI, M., I. AGUILERA, M. BIANCHI, V. E. de CARVALHO, L. O. LADEIRA, N. G. TEIXEIRA, E. A. SOARES, C. FRIEDRICH, S. BLÜGEL and Hofmann P. Bulk band structure of Bi_2Te_3. *Physical Review B*. 2014, vol. 90, 075105.

[31] DRABBLE, J R and R WOLFE. Anisotropic Galvanomagnetic Effects in Semiconductors. *Proceedings of the Physical Society. Section B*. 1956, vol. 69, no. 11, 1101–1108.

[32] KÖHLER, H. Non-parabolic E(k) Relations of the Lowest Conduction Band in Bi_2Te_3. *Phys. Stat. Sol. (b)*. 1976, vol. 73, 95.

[33] KÖHLER, H. Non-Parabolicity of the Highest Valence Band of Bi_2Te_3 from Shubnikov-de Haas Effect. *Phys. Stat. Sol. (b)*. 1976, vol. 74, 591.

[34] HILFIKER, J. N. and H. G. TOMPKINS. *Spectroscopic ellipsometry: practical application to thin film characterization*. Momentum Press, 1996.

[35] LIU, Chao-Xing, Xiao-Liang QI, HaiJun ZHANG, Xi DAI, Zhong FANG and Shou-Cheng ZHANG. Model Hamiltonian for topological insulators. *Phys. Rev. B*. 2010, vol. 82, 045122.

[36] ORLITA, M., B. A. PIOT, G. MARTINEZ, N. K. SAMPATH KUMAR, C. FAUGERAS, M. POTEMSKI, C. MICHEL, E. M. HANKIEWICZ, T. BRAUNER, S. DRAŠAR C.and Schreyeck, S. GRAUER, K. BRUNNER, C. GOULD, C. BRÜNE and L. W. MOLENKAMP. Magneto-optics of massive Dirac fermions in bulk Bi_2Se_3. *Physical Review Letters*. 2015, vol. 114, 186401.

[37] ORLITA, M., I. CRASSEE, C. FAUGERAS, A. B. KUZMENKO, F. FROMM, M. OSTLER, Th. SEYLLER, G. MARTINEZ, M. POLINI and M. POTEMSKI. Classical to quantum crossover of the cyclotron resonance in graphene: A study of the strength of intraband absorption. *New Journal of Physics*. 2012, vol. 14, 095008.

[38] LY, O. and D. M. BASKO. Theory of electron spin resonance in bulk topological insulators Bi_2Se_3, Bi_2Te_3 and Sb_2Te_3. *Journal of Physics: Condensed Matter*. 2016, vol. 28, no. 15, 155801.

[39] MIURA, Noboru. *Physics of Semiconductors in High Magnetic Fields*. Oxford University Press, USA, 2007.

[40] HAIDEMENAKIS, E. D. *Physics of Solids in Intense Magnetic Fields: Lectures presented at the First Chania Conference held at Chania, Crete, July 16–29, 1967*. Springer, 2014.

[41] ORLITA, M., P. NEUGEBAUER, C. FAUGERAS, A.-L. BARRA, M. POTEMSKI, F. M. D. PELLEGRINO and Basko D. M. Cyclotron Motion in the Vicinity of a Lifshitz Transition in Graphite. *Physical Review Letters*. 2012, vol. 108, 017602.

[42] GRIFFITHS, P. R. and J. A. de HASETH. *Fourier Transform Infrared Spectrometry, Second Edition*. John Wiley & Sons, Inc., 2006.

REFERENCES

[43] MICHELSON, Albert A. *XXVIII. Visibility of interference-fringes in the focus of a telescope* [online]. 2009. Available from: `https://www.tandfonline.com/doi/abs/10.1080/14786449108620101`.

[44] HANLEY, Q. S. Fourier Transforms Simplified: Computing an Infrared Spectrum from an Interferogram. *Journal of Chemical Education.* 2012, vol. 89, 391–396.

[45] CHRISTOPHER, C. H., G. L. CARR, R. P. S. M. LOBO, J. D. LAVEIGNE and D. B. TANNER. Silicon beam splitter for far-infrared and terahertz spectroscopy. *Applied Optics.* 2007, vol. 46, 7884–7888.

[46] WOLOS, A., S. SZYSZKO, A. DRABINSKA, M. KAMINSKA, S. G. STRZELECKA, A. HRUBAN, A. MATERNA and M. PIERSA. Landau-Level Spectroscopy of Relativistic Fermions with Low Fermi Velocity in the Bi_2Te_3 Three-Dimensional Topological Insulator. *Phys. Rev. Lett.* 2012, vol. 109, 247604.

[47] RICHTER, W. and C. R. BECKER. A Raman and Far-Infrared Investigation of Phonons in the Rhombohedral V_2-V_{13} Compounds. *Phys. Stat. Sol. (b).* 1977, vol. 84, 619.

[48] DRABBLE, J R. Galvanomagnetic Effects in p-Type Bismuth Telluride. *Proceedings of the Physical Society.* 1958, vol. 72, no. 3, 380–390.

[49] MALLINSON, R. B., J. A. RAYNE and R. W. URE. de Haas-van Alphen Effect in n-Type Bi_2Te_3. *Phys. Rev.* 1968, vol. 175, 1049–1056.

[50] KÖHLER, H. Anisotropic g-Factor of the Conduction Electrons in Bi_2Te_3. *physica status solidi (b).* 1976, vol. 75, no. 1, 127–136.

[51] DUBROKA, A., O. CAHA, M. HRONČEK, P. FRIŠ, M. ORLITA, V. HOLÝ, H. STEINER, G. BAUER, G. SPRINGHOLZ and J. HUMLÍ ČEK. Interband absorption edge in the topological insulators $Bi_2(Te_{1-x}Se_x)_3$. *Physical Review B.* 2017, vol. 96, 235202.

[52] BURSTEIN, Elias. Anomalous Optical Absorption Limit in InSb. *Phys. Rev.* 1954, vol. 93, 632–633.

[53] ORLITA, M., K. MASZTALERZ, C. FAUGERAS, M. POTEMSKI, E. G. NOVIK, C. BRÜNE, H. BUHMANN and L. W. MOLENKAMP. Fine structure of zero-mode Landau levels in $HgTe/Hg_xCd_{1-x}Te$ quantum wells. *Phys. Rev. B.* 2011, vol. 83, 115307.

[54] ASSAF, B. A., T. PHUPHACHONG, E. KAMPERT, V. V. VOLOBUEV, P. S. MANDAL, J. SÁNCHEZ-BARRIGA, O. RADER, G. BAUER, G. SPRINGHOLZ, L. A. de VAULCHIER and Y. GULDNER. Negative Longitudinal Magnetoresistance from the Anomalous $N = 0$ Landau Level in Topological Materials. *Phys. Rev. Lett.* 2017, vol. 119, 106602.

[55] KRIZMAN, G., B. A. ASSAF, M. ORLITA, T. PHUPHACHONG, G. BAUER, G. SPRINGHOLZ, G. BASTARD, R. FERREIRA, L. A. de VAULCHIER and Y. GULDNER. Avoided level crossing at the magnetic field induced topological phase transition due to spin-orbital mixing. *Phys. Rev. B.* 2018, vol. 98, 161202.

[56] HSIEH, David, Yuqi XIA, Dong QIAN, L WRAY, JH DIL, Fedorov MEIER, J OSTERWALDER, L PATTHEY, JG CHECKELSKY, Nai Phuan ONG, et al. A tunable topological insulator in the spin helical Dirac transport regime. *Nature.* 2009, vol. 460, no. 7259, 1101.

[57] AGUILERA, Irene, Christoph FRIEDRICH and Stefan BLÜGEL. Many-body corrected tight-binding Hamiltonians for an accurate quasiparticle description of topological insulators of the Bi_2Se_3 family. *Phys. Rev. B.* 2019, vol. 100, 155147.

[58] YAN, Binghai and Anne de VISSER. Half-Heusler topological insulators. *MRS Bulletin.* 2014, vol. 39, 859–866.

[59] CHADOV, S., X.-L. QI, J KÜBLER, G. H. FECHER, C. FELSER and S.-C. ZHANG. Tunable Multifunctional Topological Insulators in Ternary Heusler Compounds. *Nature Materials.* 2010, vol. 9, 541.

[60] HOU, Z., Y. WANG, E. LIU, H. ZHANG, W. WANG and G. WU. Large low-field positive magnetoresistance in nonmagnetic half-Heusler ScPtBi single crystal. *Applied Physics Letters.* 2015, vol. 107, 202103.

[61] HIKAMI, S., A. I. LARKIN and Y. NAGAOKA. Spin-Orbit Interaction and Magnetoresistance in the Two Dimensional Random System. *Progress of Theoretical Physics.* 1980, vol. 63, 707–710.

[62] SULTANA, R., G. GURJAR, P. NEHA, S. PATNAIK and V. P. S. AWANA. Treatment of the Magneto-Conductivity of Bi2Te3 Topological Insulator. *Journal of Superconductivity and Novel Magnetism.* 2018, vol. 31, 2287–2290.